Adv. Electron. Mater. **2017**, *1700464,* **DOI:** 10.1002/aelm.201700464

The Impact of Molecular *p*-Doping on Charge Transport in High Mobility Small-Molecule/Polymer Blend Organic Transistors

*Alexandra F. Paterson, Yen-Hung Lin, Alexander D. Mottram, Zhuping Fei, Muhammad R. Niazi, Ahmad R. Kirmani, Aram Amassian, Olga Solomeshch, Nir Tessler, Martin Heeney, Thomas D. Anthopoulos**

Dr. A. F. Paterson, Muhammad R. Niazi, Ahmad R. Kirmani, Prof. A. Amassian, Prof. T. D. Anthopoulos
King Abdullah University of Science and Technology (KAUST)
Physical Sciences and Engineering Division (PSE)
King Abdullah University of Science and Technology
Thuwal 23955-6900, Saudi Arabia
E-mail: thomas.anthopoulos@kaust.edu.sa

Dr. Y.-H. Lin, Dr. A. D. Mottram
Department of Physics and Centre for Plastic Electronics,
Imperial College London,
South Kensington, London SW7 2AZ (UK)

Dr. O. Solomeshch, Prof. N. Tessler
Sara and Moshe Zisapel Nano-Electronic Center
Department of Electrical Engineering
Technion - Israel Institute of Technology
Haifa 3200, Israel

Dr. Zhuping Fei, Prof. M. Heeney
Department of Chemistry and Centre for Plastic Electronics
Imperial College London
South Kensington, London SW7 2AZ (UK)

Keywords: molecular doping; organic thin-film transistors; small molecule polymer blends; hole mobility; solution processing

Abstract

Molecular doping is a powerful tool with the potential to resolve many of the issues currently preventing organic thin-film transistor (OTFT) commercialisation. Yet the addition of dopant molecules into organic semiconductors often disrupts the host lattice, introducing defects and therefore harming electrical transport. New dopant-based systems that overcome these practical utilisation issues, whilst still reaping the electrical performance benefits, would therefore be extremely valuable to the world of OTFTs. Here, we investigate the impact of *p*-doping on the charge transport in small-molecule/polymer blends consisting of the small-molecule 2,7-dioctyl[1]benzothieno[3,2-b][1]benzothiophene (C_8-BTBT), the polymer indacenodithiophene-benzothiadiazole (C_{16}IDT-BT) and the molecular dopant $C_{60}F_{48}$. Electrical field-effect measurements indicate that *p*-doping not only enhances the average saturation mobility values from 1.4 cm^2/Vs to an average of 7.8 cm^2/Vs over 50 devices (maximum values from around 4 cm^2/Vs to 13 cm^2/Vs), but also improves the other important figures of merit, namely bias-stress stability, parasitic contact resistance, threshold voltage and the overall device-to-device performance variation. Importantly, materials characterisation using X-ray diffraction, X-ray photoemission spectroscopy and ultraviolet photoemission spectroscopy, combined with charge transport modelling, reveal that effective doping is achieved without perturbing the microstructure or morphology of the polycrystalline semiconductor film. This work highlights the remarkable potential of ternary organic blends as a simple platform for OTFTs to achieve all the benefits of doping, with none of the drawbacks.

1. Introduction

The dream of organic thin-film transistors (OTFTs) in commercially available flexible, low-cost, printed electronics will only become a reality once a number of performance, stability and reproducibility related issues have been addressed. [1] One crucial figure of merit for OTFT performance is the mobility; in recent years, OTFT mobility values have made remarkable improvements, not only surpassing amorphous silicon, but also surpassing the benchmark mobility of 10 cm^2/Vs, pushing OTFTs into the realm of industrial application. [2] [3] [4] [5] Given the impressive progress that has been made in terms of mobility values, focus is now turning towards a variety of other OTFT operational hurdles. One of those operational hurdles is contact resistance, R_C, which is known to severely reduce the performance of OTFTs, by suppressing

the applied bias potential across the channel due to the potential barriers at the source and drain electrodes; [6] not only is R_C a serious disadvantage for the future downscaling of OTFTs channel dimensions, but recent work has elucidated that R_C is at the heart of the mobility overestimations in some reported high performance OTFTs. [7] [8] Other operational hurdles include the precise control of the threshold voltage, V_T, as the latter is a fundamental requisite for successful application in advanced integrated circuits. [9] [10] [11] In addition, lifetime stability is an indispensable criterion; OTFT instability manifests as a shift in V_T and a change in the on-current, I_{ON}, with the application of gate and/or drain voltage over time, known as the bias-stress effect. [12] [13] [14] Bias-stress is attributed to charge trapping during device operation [11] [15] [16] [17] [18] either in the dielectric, at the semiconductor/dielectric interface, at grain boundaries or within the bulk semiconductor. [19] [20] [21] Only when all of these parameters have been addressed, in tandem with reliable high mobility values and high density patterning, will OTFTs be seen as a competitive, viable option for use in future low-cost, plastic-based microelectronics. Any approach that can simultaneously resolve most of, if not all of, these issues, is likely to be crucial for the future of OTFTs.

One illustrious technique that offers great promise is doping. Doping has been established as a powerful tool for modern electronics for many years; not only has this technique revolutionised inorganic electronic technology by allowing conduction to be controlled in silicon[22], but the field of organic electronics originated from doping-controlled conductivity in polyacetylene[23] [24]. Doping has since matured in many areas of organic electronics, being key for the successful development of efficient organic light emitting diodes (OLEDs)[22] [25] [26] and organic photovoltaics (OPVs). [27] [28] [29] For OTFTs, molecular doping offers an exclusive opportunity to rectify the operational hurdles currently preventing their commercialisation. For example, it has been shown in the literature that doping can improve bias-stress stability and threshold voltage by deactivating charge trapping sites [16] [30] [31], improve contact resistance by reducing the width of the depletion layer at the metal/semiconductor interface [32] [33] [34] [35]

[36], and enhance mobility by increasing charge carrier density and improving energetic disorder. [37] [9] [32]

Yet despite the promises of doping and its potential impact on OTFT performance, [32] [38] [39] [40] [41] [42] [43] the introduction of even a small number of dopant molecules can easily disrupt the formation of an organic semiconductor (OSC) host lattice, introducing new microstructural defects which can reduce charge carrier mobility and offset any desired benefits. [25] This severely hinders the practical implementation of molecular doping. [44] Identifying new dopants, doped systems and doping strategies that promote high performance OTFTs, without perturbing the microstructure of the OSC and hence negatively effecting charge transport, are therefore highly sought after. [32]

In our earlier work we describe the development of ternary organic small-molecule/polymer semiconducting blends for OTFT applications, the so-called third-generation (3G) blend systems; specifically, a new blend based on the small-molecule 2,7-dioctyl[1]benzothieno[3,2-b][1]benzothiophene (C_8-BTBT), the polymer indacenodithiophene-benzothiadiazole (C_{16}IDT-BT) and the molecular dopant $C_{60}F_{48}$ (**Figure 1a**). [5] In recent years, binary organic blends that combine the superior mobility of a small-molecule [45] [46] [47] with the film-forming qualities of a polymer [47] [48] have become popular for OTFT applications because of the remarkable effects gained from this simple technique [49] [50], such as improved film formation, liquid-liquid phase separation favouring stratification of the polymer and small-molecule layers, interfacial trap density reduction and grain boundary passivation. [51] [52] Our 3G blend development highlighted an additional property of the blend, whereby the introduction of a third component, a molecular *p*-dopant, into a traditional binary small-molecule/polymer blend dramatically improves the electrical properties by reducing energetic disorder (**Figure S1** is representative of the effects of molecular doping on 3G blend OTFT characteristics). Most notably, we showed that optimised

C_8-BTBT:C_{16}IDT-BT blend TFTs *p*-doped with 1% molar weight (mol. wt.) $C_{60}F_{48}$ achieved exceptional hole mobility values in excess of 13 cm^2/Vs. [5]

Here, we show that the molecular dopant in this 3G blend system can not only dramatically improve mobility, but also has a remarkable all-round effect on OTFT performance, by improving bias-stress stability while reducing the parasitic contact resistance, threshold voltage and the overall device-to-device parameter variation. We also find that, unusually, the inclusion of the dopant does not adversely affect the nature of the C_8-BTBT crystal packing at the OTFT channel. This is a surprising result, especially considering that we have purposefully employed a simple doping technique, in-line with the concept of low cost plastic electronics, whereby the dopant is directly introduced into the semiconducting blend. Overall, the work provides unique insights into the impact of molecular doping in blend OTFTs, whilst highlighting its multiple advantages for the development of next-generation organic microelectronics.

2. Results and Discussion

2.1. Electrical Field-Effect Measurements

Because electrical field-effect measurements offer a wealth of information about doping mechanisms in semiconductor systems, we began by studying the effects of molecular doping on the OTFT transfer characteristics. The top-gate, bottom contact (TG-BC) transistor architecture (**Figure 1b**) was employed to study the optimised C_8-BTBT:C_{16}IDT-BT blend [5] doped at 0%, 0.05%, 0.1%, 0.5%, and 1% molar weight (mol. wt.) $C_{60}F_{48}$. Due to the large electron affinity of $C_{60}F_{48}$[5], electron transfer from the highest molecular orbital (HOMO) energy level of C_8-BTBT and/or C_{16}IDT-BT to the dopant's lowest unoccupied molecular orbital (LUMO), would be expected to occur (**Figure 1c**). In such *p*-doped channels there are

several things one would expect to observe in the transistor's transfer characteristics, including: an overall increase in the channel current, a shift in V_T to more positive gate voltages and suppression of any electron transport.[16] **Figure 1d** shows representative transfer characteristics for 0%, 0.05%, 0.1%, 0.5% and 1% mol. wt. $C_{60}F_{48}$ devices with channel length and width 80 µm and 1000 µm respectively. There is a clear trend of parameter changes occurring as expected, in the transfer characteristics with increasing levels of dopant concentration. The increase in current is associated with an increase in charge carrier density due to extrinsic doping of the semiconducting blend. [16] [53] The dopant can also be seen to act as an electron trap (see the energy band diagram in **Figure 1c**); for example, at lower doping percentages (0, 0.05 and 0.1%) electron transport can be observed manifested as the V-shaped transfer characteristics occurring between gate bias of -10 and 0 V, but at the higher doping percentages (0.5 and 1%) the devices are predominantly *p*-type, indicating that if the doping concentration is high enough, then the $C_{60}F_{48}$ molecules will tend to trap any mobile electrons in the channel due to their deep LUMO energy level. Furthermore, **Figure 1e** shows the evolution of $\sqrt{I_D}$ with doping ratio, demonstrating an increase in I_D and a shift in V_T in good agreement with the theoretically predicted behaviour.

Following evaluation of the single transfer characteristics, 10 transistors with channel lengths ranging from 30 µm to 100 µm, at a fixed width of 1000 µm, were measured and linear mobility, μ_{lin}, saturation mobility μ_{sat}, V_T, on-voltage, V_{ON}, on-off ratio, $I_{ON/OFF}$ and subthreshold slope, *SS*, were analysed for each doping concentration (0, 0.05, 0.1, 0.5, and 1% mol. wt.). This analysis allows us to examine the statistical trends over multiple transistors and batches. The results are presented in **Table S1** and **Figure S2**, where numerical and graphical data representations give a clear idea of parameter spreads and trends with varying doping concentration, revealing that molecular doping has a great impact. Firstly, and one of the most striking effects in this system, is the dramatic improvement in mobility with doping concentration (**Figure 1f**). Molecular doping can increase conductivity in OTFTs by several

orders of magnitude by screening charge traps in the system through the generation of excess mobile charges [54] [55], which is observable as an increase in the current at all gate voltages, and an increase in the off-current. [23] [16] [56] [57] Trap state passivation is beneficial because it reduces the resistance, and hence associated Ohmic losses in the bulk of the OSC [23] [44], as well as corresponds to an increase in the carrier mobility. For this particular blend system, the average saturation mobilities do not show any great change at the lower doping ratios of 0.05% and 0.1% for which the average μ_{sat} values are 1.9 cm^2/Vs and 1.6 cm^2/Vs respectively. Although a slight increase of μ_{sat} to 2.7 cm^2/Vs is achieved at 0.5%, in accordance with previous results, [5] the statistically critical improvements come at 1% mol. wt. doping concentration, for which the average value over 10 TFTs increases to 8.2 cm^2/Vs (**Figure 1f** and **Table S1**). The observation of statistical mobility improvement with the addition of the dopant was confirmed in even more detail by measuring 50 TFTs for each of the pristine and optimized *p*-doped blend OTFTs. **Figure S3** shows box and whisker plots for the linear and saturation mobilities of the two blends, with the whiskers being the 10-90 percentiles; **Figures S4**, **S5** and **S6** show a range of example OTFT characteristics for the 1% mol. wt. $C_{60}F_{48}$ blend system, representative of the best performing device and upper quartile, the median performers, and the lower quartile and minimum mobility values, respectively. In terms of the statistical average values, from 50 OTFTs, the average saturation mobility for the pristine blend is ≈1.4 cm^2/Vs compared to an average of ≈7.8 cm^2/Vs for the doped blend. The maximum mobilities for the pristine and doped blends are ≈4.2 cm^2/Vs and ≈12.8 cm^2/Vs respectively. A similarly strong trend is also seen with the linear mobilities, where the average linear mobility for the pristine blend of ≈1 cm^2/Vs increases to an average of ≈5.3 cm^2/Vs for the doped blend.

Secondly, the data indicates that there is a noticeable improvement in device uniformity with intentional doping. A narrow parameter spread, or an approach for improving the distribution of parameters, is important for integrated circuitry where a large number of devices are combined on the same circuit.[11] [58] Here, the most noticeable difference is at 0.5% $C_{60}F_{48}$,

where the device uniformity is improved for μ_{lin}, μ_{sat}, V_{ON}, V_T, SS and $I_{ON/OFF}$. Although $I_{ON/OFF}$ (**Figure S2e**) and SS (**Figure S2f**) improve in terms of parameter spread, they are the only parameters that do not seem to be strongly affected by doping. One possible reason for this is that some of the underlying issues for improving the values of $I_{ON/OFF}$ and SS lie outside the capacity of the bulk semiconductor. Therefore, although it is theoretically possible that molecular doping can impact $I_{ON/OFF}$ by increasing conductivity [39] [40] and improve SS by filling shallow trapping sites, [11] it may not affect these two parameters with the same degree as the other characteristics. Both parameters can be addressed by considering alternative aspects of device engineering, such as the dielectric layer [59] and the semiconductor/dielectric interface.[60]

Finally, V_T and V_{ON} are shown to have a strong correlation with dopant concentration (**Figure 2a**), with both shifting towards more positive voltages with increasing concentration. In an ideal OTFT, there are no trap states and mobile charge carriers increase as soon as V_G passes the flat-band voltage (V_{FB}); this is often indicated by V_{ON}. In this ideal situation, the addition of a molecular dopant to a system will increase the number of background carriers. The impact of this would be seen as both an increase in the off-current (depending on the degree of doping), and a shift in the V_{ON} and V_T to more positive voltages (for a *p*-type semiconductor). But in reality, trap states exist in organic semiconductors, and cause an increased separation between V_{ON} and V_T, resulting in more extreme (i.e. negative for *p*-type semiconductors) values of V_T. In the scenario whereby traps exist, the addition of the dopant will still cause a shift in V_{ON}, but it will also have an additional effect manifested as a decreasing gap between V_{ON} and V_T, due to the passivation of trap states at deeper energies. [56] This allows a channel to be formed at lower gate voltages. **Figure S2** demonstrates a decrease in the gap between V_{ON} and V_T with the addition of $C_{60}F_{48}$ in the C_8-BTBT:C_{16}IDT-BT blend, indicating that the $C_{60}F_{48}$ has donated holes to deep trap states present in the system [11] [9], passivating the charge traps and allowing the TFTs to switch on quickly and efficiently when a gate bias is applied.

Taking a close look at V_T is therefore not only important for practical implications, but also offers valuable information about doping mechanisms. Because V_T is the voltage required to fill deep trap states before mobile charge carriers can be induced at the channel [61] [62] [63], the observed shift in V_T can be used to approximate the total number of holes, Δh^+, induced by the $C_{60}F_{48}$ to the channel with the following equation:

$$\Delta h^+ = \frac{C_i \left| V_{\mathrm{TH(pristine)}} - V_{\mathrm{TH(doped)}} \right|}{e} \quad (1)$$

where C_i is the geometric capacitance of the dielectric layer and e is the charge of an electron. **Figure 2b** is a graphical representation of the number of donated holes with the doping ratio, which follows a steady increase up to 0.5% $C_{60}F_{48}$ before starting to plateau towards 1%.

2.1.1. Bandgap Density of States Analysis

It is expected that efficient doping would cause a shift in the density of states (DOS) with respect to (w.r.t.) the Fermi energy (E_F) due to changes of the state occupancy as compared to the pristine semiconductor. To investigate this further, we employed the Grünewald analysis scheme to compare the doped and pristine 3G blend systems.[64] [65] The Grünewald model is used to calculate the density of immobile states within the bandgap by comparing the field-effect accumulated charge, with the mobile charge carriers measured from the drain current, in the TFT transfer characteristics.[64] [65] A full derivation of the model may be found in the original article by Grünewald *et al.*;[65] this derivation results in three fundamental equations, which enable the calculation of the DOS within the bandgap as a function of energy away from the thermal equilibrium Fermi level (i.e. the Fermi level of the device at flat band voltage). For simplicity, we define the field-effect voltage (V_F) as the applied gate voltage above flat-band voltage. Since the flat-band voltage is often assumed to be the turn-on voltage (V_{ON}), this can be calculated experimentally using ($V_F = V_G - V_{ON}$). The first equation relates the density

of accumulated charge carriers, $p(V_0)$, to both the semiconductor/dielectric interface internal potential V_0 and the field-effect voltage V_F:

$$p(V_0) = \frac{C_i^2}{q\varepsilon_s\varepsilon_0} V_F \left(\frac{\mathrm{d}V_0}{\mathrm{d}V_F}\right) \quad (2)$$

where q is the elementary charge, ε_s is the relative permittivity of the semiconductor and ε_0 is the permittivity of free space. To calculate the values for accumulated charge, a relationship between the surface potential and field-effect voltage is required. The Grünewald method provides the following equation:

$$\exp\left(\frac{qV_0}{k_BT}\right) + \frac{qV_0}{k_BT} - 1 = \frac{qC_id_s}{k_BT\varepsilon_s\varepsilon_0 I_{off}} [I_D(V_F)V_F - \int I_D(V_F)\mathrm{d}V_F] \quad (3)$$

where k_B and T are the Boltzmann constant and temperature respectively, and d_s is the thickness of the semiconductor. From Equation (2) a numerical function of $V_0(V_F)$ can be created and then inserted into Equation (1). The accumulated charge carriers as a function of the internal potential $p(V_0)$ is a convolution of the density $g(E)$ with the Fermi-Dirac distribution. There are multiple available techniques for deconvoluting the latter two functions, where the most basic choice is to use the zero temperature approximation to simplify the relationship to the following differential [64]:

$$g(E) \approx \frac{1}{q}\frac{\mathrm{d}}{\mathrm{d}V_0}[n(V_0)] \quad (4)$$

The Grünewald analysis scheme has been successfully applied by Hunter *et al*. to similar small-molecule/polymer blend systems in the literature. [66] Because of the similarity between our system and the previously reported work, the justification of the key approximations by

Hunter *et al*. remain applicable and have therefore been used as a basis for our analysis. Further information can be found in the references.[66]

Figure 2c shows the results from the bandgap analysis for the 3G blend doped at 0, 0.05, 0.1, 0.5 and 1 % mol. wt. $C_{60}F_{48}$. Here, we see that all densities of states overlap, except for the 1 % mol. wt. ratio blend, which exhibits a shift and an increase in the number of states compared to the other four results. A negative shift in the energy w.r.t. E_F is indicative of *p*-doping, as the thermal equilibrium Fermi energy level approaches the HOMO level, shifting the measured DOS towards higher energy w.r.t. E_F. The absence of any shift in the DOS at lower doping concentrations is most likely attributed to the presence of deep traps that pin E_F, a process that has been described previously.[57] Another indication of doping is the increase in the channel's off-current (I_{OFF}) seen in the linear transfer characteristics due to the increase in the background conductivity of the semiconductor (**Figure S7**). Here we will only consider I_{OFF} as measured in the linear operating regime, as at high drain voltages, i.e. in the saturation regime, I_{OFF} is also affected by the gate leakage. Interestingly, I_{OFF} for the pristine (0 %) and lightly *p*-doped (i.e. 0, 0.05 and 0.1 %) OTFTs are approximately equal, and increases only for the higher dopant concentrations (e.g. 0.5 and 1 %). Although the apparent independence of I_{OFF} to dopant concentration in this low doping range may appear somewhat surprising, it is in agreement with previously published results that have been ascribed to the pinning of E_F. [57]

There are four possible reasons that could explain the increasing channel on-current (I_{ON}) in the transfer characteristics, along with both the lack of observable increase in the linear regime I_{OFF} and lack of observable shift in the DOS for the 0-0.5% mol. wt. doped devices: (i) although the doping is shifting the Fermi level closer to the HOMO edge with increasing $C_{60}F_{48}$ concentration, it is obscured by the experimental noise floor and therefore undetectable, as the DOS analysis is highly sensitive to the measurement of I_{OFF}; (ii) the concentration of the excess holes induced by the dopant molecules at low concentration is not high enough to deactivate all deep traps, therefore the Fermi energy remains pinned [57] and only once all trap

have been filled, i.e. at the highest doping concentration, a shift in the DOS w.r.t. E_F can be observed; (iii) for 0-0.5% mol. wt. doping concentrations the Fermi level shift is negligible and the increase in current is due to an enhancement of the mobility most likely due to the screening of hole trap states, and (iv) the effect is a combination of both the noise floor obscured doping and mobility enhancement. The most likely explanations for the lack of an observable shift are that the change in energy of the thermal equilibrium Fermi level from 0-0.5% mol. wt. is too small to be measured using the analytical techniques employed here, or that there is no shift in the DOS due to the Fermi level being pinned at the trap level for the low doping concentrations.

2.1.2. Bias-Stress Effect

The systematic shifts observed in V_T and DOS implies that the $C_{60}F_{48}$ is indeed filling hole trap states present in the pristine C_8-BTBT:C_{16}IDT-BT blend. Charge trapping may occur at the contacts, bulk or the dielectric/semiconductor interface [67] [68] [69] [70] and can dramatically influence the operational stability of the device. [16] [71] The impact of charge trapping on OTFT operational instability is severe for real-life applications outside the laboratory. For example, if OTFTs are used to drive OLEDs in active-matrix OLED (AMOLED) displays, the brightness of the display will deteriorate over time if there is a decline in I_{ON}.[14] It is therefore a fundamental requirement that OTFTs are stable throughout the duration of their expected use, and processes for filling, or in other words deactivating, unwanted trap states are highly desirable.

To investigate whether intentional doping in the 3G blend has indeed resulted in deactivation of charge trapping sites that are responsible for bias-stress instability, both the pristine and the best performing doped blend were investigated and compared in bias stress stability tests. OTFTs with channel length 80 µm and width 1000 µm for both blends were subjected to 20,000 s of constant gate bias (V_G = -40 V) and constant drain bias (V_G = -10 V) in

a nitrogen atmosphere. At the end of the bias-stress tests, the drain current measured at V_G = 60 V had deteriorated by 17.7 % for the pristine blend, and deteriorated by 4.2 % for the best performing blend (**Figure 3a** and **3b**, respectively). The change in threshold voltage after stressing was $\Delta V_{T\_pristine}$ = -1.34 V for the pristine blend and ΔV_{T_doped} = -0.91 V for the doped blend. Therefore, there are only slight changes in the performance parameters over time for both systems, with the doped blend exhibiting significantly smaller changes as compared to the original state.

To compare the 3G blend system to other available systems, a summary of the literature on bias-stress stability for blend OTFTs is collated in **Table 1**. It can be seen that the 3G blend performs extremely well; both the pristine and doped blends have been stressed for a comparatively substantial period of time, yet they are able to maintain similar performance levels throughout the duration of the bias-stress tests. This is very promising and, in particular, the best performing doped blend has a high mobility and hence high drain current, which makes it particularly attractive for a range of electronic applications.

Figure 3c shows the experimental data from the stress-bias measurements, where the V_T shift/instability of both blends appears to saturate over time. This is expected from such measurements due to a reduction in the trapping rate as the trap states become occupied. To quantify the bias-stress effect in the two blend systems, we fitted a stretched exponential function to the experimental data using:[1] [20] [72]

$$\Delta V_{\mathrm{T}}(t) = \Delta V_0 \left\{1 - \exp\left[-\left(\frac{t}{\tau}\right)^{\beta}\right]\right\} \quad (5)$$

where $\Delta V_0 = V_G - V_{T\_initial}$, with $V_{T\_initial}$ being the threshold voltage prior to bias stress, τ is the relaxation time and β is the stretching parameter with a value between 0 and 1. The stretched exponential fittings are shown as dashed lines in **Figure 3c** and have been used to extrapolate

the β and τ parameters. For the doped system, the stretching parameter is $\beta_{doped} = 0.58$ and the relaxation time is $\tau_{doped} = 1\times10^7$, compared to a stretching parameter of $\beta_{pristine} = 0.29$ for the pristine system and a relaxation time of $\tau_{pristine} = 7\times10^8$. The coefficient of determination, R^2, is 0.947 and 0.946 for the doped and pristine systems respectively. A greater value of β (i.e. β closer to 1) for the doped system compared to the pristine system indicates a less stretched bias-stress response time, i.e. a more uniform distribution of trapping sites near the HOMO level (shallow traps) [73]. In addition, the relaxation time, τ, is seen to decrease with the addition of $C_{60}F_{48}$, implying that hole trapping within the doped system happens on a shorter timescale. These results suggest that *p*-doping of the blend deactivates deep traps, leaving behind energetically shallower traps to dominate conduction in the channel. The latter conclusion is also in line with the reduced V_T values observed for the best performing doped blend (**Figure S2c**). The fact that intentional *p*-doping of the blend semiconductors can influence the operating stability of the resulting OTFTs has extremely valuable practical implications, the benefits of which will be fully analysed in the future.

2.1.3. Contact Resistance

To conclude the overall picture of how the *p*-dopant influences the operating characteristics of the 3G ternary blend system, we investigated its impact on the contact resistance. R_C is well known to have a tremendous and unfavourable influence on OTFT operation, especially in short channel devices [74] [75]; therefore reducing R_C is not only important for OTFT operation and mobility values, but is also highly important for OTFT miniaturisation [7] and accurate parameter analysis.[7] [76] One key technique that has been highlighted for reducing contact resistance in OTFTs is via intentional doping of the critical semiconductor-contact interface.[77] [33] [34] [35]. The scaling law method that is often used to estimate the contact resistance values from the OTFT output characteristics is the transmission line method (TLM) and relies on the following linear expression:[78]

$$R_{\mathrm{ON}} = \frac{\partial V_{\mathrm{D\_lin}}}{\partial I_{\mathrm{D\_lin}}} = r_{\mathrm{channel}} L + R_{\mathrm{C}} \quad (6)$$

where L is the channel length, R_{ON} is the total device resistance measured (i.e. drain/source and channel resistance) as a function of L, $r_{channel}$ is the resistance across the channel and R_C is the resistance at the S/D contacts. Measurements were taken from OTFTs with channel lengths ranging from 20 to 200 µm for the C_8-BTBT:C_{16}IDT-BT blend with $C_{60}F_{48}$ doping concentrations of 0, 0.05, 0.1, 0.5 and 1% mol. wt. The contact resistance (R_CW) values were calculated as a function of V_G and the results are shown in **Figure 4**. There is a strong relationship between molecular doping and contact resistance; it is also clear that R_C is dependent on gate voltage, which is expected for this type of TG-BC staggered architecture.[79] [80] The largest effect on R_C is between 0 and 0.1% mol. wt. $C_{60}F_{48}$, where the contact resistance is reduced by 82.5% from $R_C \approx 263$ kΩ to $R_C \approx 46$ kΩ (R_C is taken from V_G = -50 V). When the doping is increased to 1% mol. wt. R_C is reduced further to ≈16 kΩ. Along with the donation of charge carriers to deep trap states, the improvement in R_C highlighted in these results offers another explanation for the superior transistor characteristics in the best performing blend compared to the pristine blend.[16]

2.2. Materials Characterisation

So far, molecular *p*-doping effects on electrical characteristics have been considered. But another important question to ask is: *have the dopant molecules introduced structural defects and disrupted the packing motif of the host semiconductor*? This is a key consideration, because the quality and ordering of the semiconductor microstructure can determine and/or influence OTFT performance, as the introduction of structural defects can result in charge trapping. [59] [81] [82] Despite the positive attributes associated with the blend approach adopted here, bulk doping

of solution processed organic semiconducting channel is infrequently used because of the likelihood of disrupting the long range crystallinity of the layer. Instead, a range of different doping methods are typically employed to avoid introducing such defects, including contact doping [83] [33] [84] [85] [34] [86] [87], interlayer doping [88] and chemical vapour doping [89] [90]. However, techniques like these can be complicated to fabricate, hence costly to scale-up, or difficult to control, and can tend to focus specifically on improving one OTFT parameter. For realising OTFTs in inexpensive microelectronics, doping protocols that are simple and easy to implement, yet do not change the organic semiconducting layer, are essential and hence highly desired.[32]

To that end, we now turn our focus onto the impact that the $C_{60}F_{48}$ has had on the microstructure of the C_8-BTBT:C_{16}IDT-BT blend. The first step taken to explore the microstructure with doping concentration was using polarised optical microscopy (POM). **Figure 5** shows the C_8-BTBT:C_{16}IDT-BT layers with $C_{60}F_{48}$ at 0 (**a**), 0.05 (**b**), 0.1 (**c**), 0.5 (**d**) and 1 % (**e**) mol. wt. Although there is some variation in the morphology due to the intrinsic nature of the films, there is very little difference between these images. After studying a number of blend films for each doping concentration, the dopant appears to have no noticeable effect on the crystalline domains.

Another interesting observation is the high density of "agglomerates" distributed within all of the blend films, regardless of the presence/amount of dopant (highlighted in **Figure 5**). These agglomerates, or defects, would be expected to behave as charge trapping centres, severely limiting charge transportation and hence the performance of OTFTs. Therefore, to achieve remarkably high mobilities of 12.8 cm^2/Vs with this morphology is certainly surprising. [91] [92] [93] [94] [95] The poor morphology may offer another explanation as to why the system exhibits significant energetic disorder in the first place.[5] [96] The agglomerations will also affect the quality of the semiconductor/dielectric interface and therefore may shed some light on the *SS* values discussed earlier; the fact that the morphology remains unchanged at the

semiconductor/dielectric interface with the addition of the dopant may also explain why there is no improvement in *SS*, even though there is a dramatic difference in μ_{lin}, μ_{sat}, V_{ON}, and V_T. The poor morphology highlights two other key points regarding this system: (i) the powerful role that the *p*-dopant is playing in this 3G organic blend system, and (ii) the potential that this system could have with further optimisation to remove the agglomerations and improve the thin-film morphology.

The crystal structure and molecular packing of the blend layers was also investigated using grazing incidence wide angle X-ray scattering (GIWAXS), which is shown in **Figure 6**. The blend layers investigated contain $C_{60}F_{48}$ at 0, 0.1, 1 and 5 % mol. wt., with the latter concentration (5 %) being included for the GIWAXS studies as higher doping concentrations are more likely to introduce structural disorder.[97] [98] The blend films were investigated at various grazing incidence angles (0.05°, 0.10°, 0.15°) with the critical angle found to be 0.15°. All of the blend films are found to exhibit high lamellar ordering, irrespective of the dopant concentration, which is shown by the presence of (00*l*) peaks (*l* = 1, 2, 3) with interplanar spacing of *d* = 2.8 nm for (001) Bragg Sheet (q_z = 2.23 nm^{-1}) (**Figure S8**); this predominant out of plane ordering is consistent with published C_8-BTBT literature.[99]

In **Figure S9**, intensity versus q_z has been plotted for two different angles of incidence, one of which is below the critical angle (0.10°) and the other is the critical angle (0.15°). This data not only highlights that the dopant does not affect the crystallinity of blend films, but also provides information about the vertical profiling of the doped blends, specifically the qualitative composition in the top few nm of the films. **Figure S9** shows that for grazing angles below the critical incidence angle (i.e. 10°) the C_{16}IDT-BT signature at q_z = 3.63 nm^{-1} is not present, but in **Figure S9** it is present at 0.15°. This suggests that the polymer is not present in the top few nm of the film and that it has segregated to the bottom of the film for all of the doping concentrations. This observation correlates with the typical vertical phase separation of a

small-molecule and a polymer as featured in numerous pieces of small-molecule/polymer organic blend literature.[5] [50] [79]

The in-plane structures of the blend films were also investigated. **Figure 6a** compares the q_{xy} position for all of the films, with the dashed line highlighting the fact that there is no shift in the in-plane peak position for any of the blend films investigated. This finding is also corroborated by **Figure 6b** which shows that there is also no shift in the q_z values for the blend films at any dopant concentration. Overall, the GIWAXS data indicates that the packing of the C_8-BTBT at the surface/air interface has not been altered by the presence of the $C_{60}F_{48}$ dopant.

To further investigate the impact of $C_{60}F_{48}$ doping on the composition and electronic properties of the blend, we used photoemission spectroscopy (PES) to look at the chemical composition of the surface of the blend films as it has been previously shown to provide valuable information.[100] [56, 101] [102] Firstly, ultra-violet photoemission spectroscopy (UPS) was used to measure secondary-electron (SE) cutoffs (**Figure 7a**) and valance band minima (VBM) (**Figure 7b**) for the pristine C_8-BTBT:C_{16}IDT-BT and best performing *p*-doped C_8-BTBT:C_{16}IDT-BT:$C_{60}F_{48}$(1%) ternary blend layers. The VBM data was added to the optical band gap of the blend (1.5 eV) to calculate the conduction band minima (CBM) for each blend. The results were then used to draw the energy band diagram shown in **Figure 7c**. For the sake of simplicity we have only drawn the band structures for the pristine blend and compared to that of the 1% mol. doped (best performing) blend. As can be seen, the data suggests that the Fermi level, E_F, moves towards the VBM by ≈0.1 eV with the addition of the $C_{60}F_{48}$ dopant. It is expected that the shift is reasonably small in magnitude; organic materials tend to have a high density of in-gap trap states, therefore doping these materials leads to Fermi level pinning inside the band gap, resulting in smaller E_F shifts. [56] [57] [103] This data indicates successful *p*-doping, which, along with the field-effect measurements, further demonstrates that doping mechanisms are responsible for the improvement in the OTFT characteristics.

Finally, X-ray photoemission spectroscopy (XPS) was used to measure the chemical composition at the surface of the blend films, i.e. at the TG-BC channel, with the aim of elucidating the POM and GIWAXS data presented earlier. **Figure S10** shows the XPS survey spectra for the pristine (**a**) and best performing 1% mol. wt. $C_{60}F_{48}$ (**b**) blend films, where S2p and C1s core levels appear as the main peaks for both samples. **Table S2** summarises the relative atomic concentrations for the blend films; remarkably, there is no difference between the two films, with no F-signal (associated with the $C_{60}F_{48}$) being detected at the surface of the best performing *p*-doped ternary blend. This data suggests that the dopant molecules are distributed towards the middle and/or bottom of the blend layer. In other words, the dopant resides in the polymer layer of the vertically phase separated film, and not in the C_8-BTBT layer presented at the surface/air interface. This observation corroborates with previous findings obtained from secondary ion mass spectrometry (SIMS) measurements.[5] It is worth mentioning the fact that such an unusual materials distribution would result in spatial separation between the dopant molecules (i.e. $C_{60}F_{48}$) and the channel region. This is perhaps the reason why the POM and GIWAXS data suggests that the crystallinity of the top C_8-BTBT layer remains unchanged for any $C_{60}F_{48}$ concentration. Yet at the same time, the field-effect, DOS and UPS data show that the blend OTFTs harness the electrical benefits associated with *p*-doping (i.e. improvements in μ and bias-stress stability, and a reduction in V_T and R_C) most likely via a remote/modulation-like doping process. [104] However, further work would be required to better understand the nature of *p*-doping starting with the elucidation of the spatial distribution of the dopant molecules across the phase separated layer. However, if such spatially separated dopant-channel system exists, the implications could be significant, as the doping efficiency of blend systems could be, in principle, further enhanced via material optimization and/or through the choice of different (one or more) molecular dopants that are distributed in a controlled manner anisotropically across the blend.

3. Conclusion

In summary, we have studied the impact of molecular *p*-doping on third-generation organic semiconducting blends comprised of C_8-BTBT:C_{16}IDT-BT using electrical field-effect measurements and several complementary materials characterisation techniques. Via simple admixing of the molecular *p*-dopant, $C_{60}F_{48}$, directly into the semiconductor blend formulation is found to have an extraordinary and positive impact on the operating characteristics of the resulting OTFTs. In particular, *p*-doped devices offer remarkably enhanced hole mobility, improved device parameter uniformity, including reduced threshold voltage, improved operating stability and reduced contact resistance; all important prerequisites for practical utilisation of any transistor technology in commercial applications. By uncovering the strong relationship between the doping ratio and V_T, comparing the stretching parameter and relaxation time extrapolated from the bias-stress data, detecting a shift in E_F via both modelling and experimental techniques, we show that the underlying reason for the dramatic improvement in the electrical characteristics is hole trap deactivation, with $C_{60}F_{48}$ donating holes to deep trap states present in the blend system. Surprisingly, this ternary blend system appears to enable efficient *p*-doping without any apparent adverse effect (e.g. introduction of defects) on the layer's crystalline microstructure that defines the transistor channel. As one of the main setbacks for doping in OTFTs is that high doping concentrations have a tendency to reduce the semiconductor crystallinity, this surprising finding is not only intriguing, but also highly relevant for the future of doping in OTFTs. [44] Finally, the study highlights the C_8-BTBT:C_{16}IDT-BT:$C_{60}F_{48}$ 3G blend system as a very attractive model system that could help in the development of simple and universal doping techniques for OTFTs.

4. Experimental Section

Material preparation: C_8-BTBT was bought from 1-Material and used as received. The C_{16}IDT-BT and $C_{60}F_{48}$ were both made in accordance with previous procedures.[105] [106] The small-molecule/polymer blend solution was prepared as previously reported, at the optimised 1/4 small-molecule/polymer ratio in a 1/2 tetralin/chlorobenzene solvent solution, at a solution concentration of 10 mg/ml. [5] A separate solution of $C_{60}F_{48}$ was prepared in chlorobenzene and added directly to the parent small-molecule/polymer blend solution, to dope the blend at 0.05, 0.1, 0.5, 1 and 5% molar weight percentage $C_{60}F_{48}$ as required. A magnetic stirrer was used to stir each of the blend solutions until the blend components had fully dissolved. To prepare blend films, the blend solutions were heated and stirred at 60°C for 15 min, before being deposited via static spin-coating in two steps: 1) 500 rpm for 10 seconds, 2) 2000 rpm for 30 seconds. The films were left for 5 minutes for excess solvent to evaporate, then annealed at 120°C for 2 minutes and quenched to room temperature

Transistor fabrication and characterisation: The blend TFTs were fabricated on 20 x 20 mm Borofloat glass substrates that were ultrasonicated in solutions of DECON90, acetone and isopropanol, in that order. 40 nm source and drain contacts made from Au were then thermally evaporated onto the glass substrate and treated with pentafluorothiophenol (PFBT) to modify the workfunction of the Au electrodes. The blend films were then heated, deposited and annealed on top of the PFBT-treated electrodes using the process described above. Polytetrafluoroethylene (PTFE) (Teflon™ AF2400) was purchased from Sigma Aldrich and used as a polymer dielectric layer. The Teflon™ AF2400 was dissolved in FC-43 solvent at a concentration of 25 mg/ml and then spin-coated in two steps: 1) 500 rpm for 20 seconds, 2) 1000 rpm for 30 seconds and then annealed at 50°C for 1 hour. This produces a Teflon™ AF2400 dielectric layer that is ≈335 nm thick, where the film thickness was measured for each set of devices using a Bruker Dektak. Finally, 50 nm thick Al contacts were thermally evaporated for the gate electrodes in the TG-BC structure. An Agilent B2902 source

measurement unit (SMU) was then used as a semiconductor parameter analyser to measure the transfer and output characteristics.

Polarised optical microscopy: Optical imaging of the various blend films was carried out using a Nikon LV-100 microscope.

Grazing incidence wide angle X-ray scattering: GIWAXS measurements were performed at D-line at the Cornell High Energy Synchrotron Source (CHESS) at Cornell University using a 0.5 mm × 0.1 mm sized beam with a wavelength of 1.15 Å. A fast area detector Dectris Pilatus 100k was used for data acquisition at a distance of 180 mm from the sample.

X-ray Photoelectron Spectroscopy: XPS measurements were carried out in an ultrahigh vacuum (UHV) Omicron chamber equipped with a SPHERA U7 hemispherical energy analyser. X-ray photons with an incident kinetic energy of 1486.6 eV from a monochromated Al K α X-ray source with a total energy resolution of 0.1 eV were used. The base pressure for the chamber during the measurements was $< 5 \times 10^{-9}$ mbar.

Ultra-violet Photoelectron Spectroscopy: For the UPS measurements, the UHV base pressure was maintained below 8×10^{-9} mbar. The photon line width was ca. 250 eV and the minimum spot size ca. 1 mm. He I photons (21.2 eV) were used to acquire the spectra at normal emission. The photoelectrons were collected by the SPHERA U7 hemispherical energy analyser with a 7 channel MCD detector, in Constant Analyzer Energy (CAE) mode. A constant bias of -10 V was applied to the sample for accurate measurement of the secondary cutoffs

Supporting Information

Supporting Information is available from the Wiley Online Library or from the author.

Acknowledgements

T.D.A. and A.F.P acknowledge financial support from Cambridge Display Technology (Company Number 2672530). O.S. acknowledges the support of the Center for Absorption in

Science of the Ministry of Immigrant Absorption under the framework of the KAMEA Program.

Received: ((will be filled in by the editorial staff))
Revised: ((will be filled in by the editorial staff))
Published online: ((will be filled in by the editorial staff))

References

[1] H. Sirringhaus, *Advanced Materials* **2014**, 26, 1319.
[2] H. Minemawari, T. Yamada, H. Matsui, J. Tsutsumi, S. Haas, R. Chiba, R. Kumai, T. Hasegawa, *Nature* **2011**, 475, 364.
[3] H. Iino, T. Usui, J.-i. Hanna, *Nature communications* **2015**, 6, 6828.
[4] W. Zhang, Y. Han, X. Zhu, Z. Fei, Y. Feng, N. D. Treat, H. Faber, N. Stingelin, I. McCulloch, T. D. Anthopoulos, M. Heeney, *Advanced Materials* **2015**, DOI: 10.1002/adma.201504092n/a.
[5] A. F. Paterson, N. D. Treat, W. Zhang, Z. Fei, G. Wyatt-Moon, H. Faber, G. Vourlias, P. A. Patsalas, O. Solomeshch, N. Tessler, M. Heeney, T. D. Anthopoulos, *Advanced Materials* **2016**, 28, 7791.
[6] M. Marinkovic, D. Belaineh, V. Wagner, D. Knipp, *Advanced Materials* **2012**, 24, 4005.
[7] T. Uemura, C. Rolin, T.-H. Ke, P. Fesenko, J. Genoe, P. Heremans, J. Takeya, *Advanced Materials* **2016**, 28, 151.
[8] E. J. Meijer, G. H. Gelinck, E. van Veenendaal, B.-H. Huisman, D. M. de Leeuw, T. M. Klapwijk, *Applied Physics Letters* **2003**, 82, 4576.
[9] J. H. Kim, S. W. Yun, B.-K. An, Y. D. Han, S.-J. Yoon, J. Joo, S. Y. Park, *Advanced Materials* **2013**, 25, 719.
[10] K. Pernstich, S. Haas, D. Oberhoff, C. Goldmann, D. Gundlach, B. Batlogg, A. Rashid, G. Schitter, *Journal of Applied Physics* **2004**, 96, 6431.
[11] A. Salleo, in *Organic Electronics*, DOI: 10.1002/9783527650965.ch14, Wiley-VCH Verlag GmbH & Co. KGaA **2013**, p. 341.
[12] H. H. Choi, M. S. Kang, M. Kim, H. Kim, J. H. Cho, K. Cho, *Advanced Functional Materials* **2013**, 23, 690.
[13] J. F. M. Hardigree, H. E. Katz, *Accounts of Chemical Research* **2014**, 47, 1369.
[14] B. Kang, H. H. Choi, K. Cho, *SID Symposium Digest of Technical Papers* **2015**, 46, 966.
[15] Y. Chen, V. Podzorov, *Advanced materials* **2012**, 24, 2679.
[16] S. Rossbauer, C. Muller, T. D. Anthopoulos, *Advanced Functional Materials* **2014**, 24, 7116.
[17] W. H. Lee, H. H. Choi, D. H. Kim, K. Cho, *Advanced Materials* **2014**, 26, 1660.
[18] S. G. J. Mathijssen, M. Colle, H. Gomes, E. C. P. Smits, B. B. de, I. McCulloch, P. A. Bobbert, L. D. M. de, *ADVANCED MATERIALS* **2007**, 19, 2785.
[19] H. Sirringhaus, *Advanced Materials* **2009**, 21, 3859.
[20] U. Zschieschang, R. T. Weitz, K. Kern, H. Klauk, *Applied Physics A* **2009**, 95, 139.
[21] S. Singh, Y. N. Mohapatra, *Ieee Electron Device Letters* **2016**, 37, 35.
[22] K. Walzer, B. Maennig, M. Pfeiffer, K. Leo, *Chemical Reviews* **2007**, 107, 1233.

[23] H. Mendez, G. Heimel, A. Opitz, K. Sauer, P. Barkowski, M. Oehzelt, J. Soeda, T. Okamoto, J. Takeya, J.-B. Arlin, J.-Y. Balandier, Y. Geerts, N. Koch, I. Salzmann, *Angewandte Chemie-International Edition* **2013**, 52, 7751.
[24] H. Shirakawa, E. J. Louis, A. G. MacDiarmid, C. K. Chiang, A. J. Heeger, *Journal of the Chemical Society, Chemical Communications* **1977**, DOI: 10.1039/C39770000578.
[25] B. Lüssem, M. Riede, K. Leo, *physica status solidi (a)* **2013**, 210, 9.
[26] X. Zhou, M. Pfeiffer, J. S. Huang, J. Blochwitz, A. Werner, K. Leo, *MRS Online Proceedings Library Archive* **2002**, 725, P9.11 (4 pages).
[27] Y. Zhang, H. Zhou, J. Seifter, L. Ying, A. Mikhailovsky, A. J. Heeger, G. C. Bazan, T.-Q. Nguyen, *Advanced Materials* **2013**, 25, 7038.
[28] I. Salzmann, G. Heimel, *Journal of Electron Spectroscopy and Related Phenomena* **2015**, 204, Part A, 208.
[29] G. K. Mor, D. Jones, T. P. Le, Z. Shang, P. J. Weathers, M. K. B. Woltermann, K. Vakhshouri, B. P. Williams, S. A. Tohran, T. Saito, R. Verduzco, A. Salleo, M. A. Hickner, E. D. Gomez, *Advanced Energy Materials* **2014**, 4.
[30] D. Khim, K.-J. Baeg, M. Caironi, C. Liu, Y. Xu, D.-Y. Kim, Y.-Y. Noh, *Advanced Functional Materials* **2014**, 24, 6252.
[31] M. P. Hein, A. A. Zakhidov, B. Lüssem, J. Jankowski, M. L. Tietze, M. K. Riede, K. Leo, *Applied Physics Letters* **2014**, 104, 013507.
[32] B. H. Lee, G. C. Bazan, A. J. Heeger, *Advanced Materials* **2016**, 28, 57.
[33] S. Singh, S. K. Mohapatra, A. Sharma, C. Fuentes-Hernandez, S. Barlow, S. R. Marder, B. Kippelen, *Applied Physics Letters* **2013**, 102.
[34] T. Minari, P. Darmawan, C. Liu, Y. Li, Y. Xu, K. Tsukagoshi, *Applied Physics Letters* **2012**, 100.
[35] A. R. Hosseini, M. H. Wong, Y. L. Shen, G. G. Malliaras, *Journal of Applied Physics* **2005**, 97.
[36] T. Miyadera, T. Minari, K. Tsukagoshi, H. Ito, Y. Aoyagi, *Applied Physics Letters* **2007**, 91, 013512.
[37] G. H. Lu, J. Blakesley, S. Himmelberger, P. Pingel, J. Frisch, I. Lieberwirth, I. Salzmann, M. Oehzelt, R. Di Pietro, A. Salleo, N. Koch, D. Neher, *Nature communications* **2013**, 4.
[38] B. Lüssem, M. L. Tietze, H. Kleemann, C. Hoßbach, J. W. Bartha, A. Zakhidov, K. Leo, *Nature communications* **2013**, 4.
[39] E. Lim, B.-J. Jung, M. Chikamatsu, R. Azumi, Y. Yoshida, K. Yase, L.-M. Do, H.-K. Shim, *Journal of Materials Chemistry* **2007**, 17, 1416.
[40] Y. Abe, T. Hasegawa, Y. Takahashi, T. Yamada, Y. Tokura, *Applied Physics Letters* **2005**, 87, 153506.
[41] J. G. Mei, Y. Diao, A. L. Appleton, L. Fang, Z. N. Bao, *J. Am. Chem. Soc.* **2013**, 135, 6724.
[42] T. D. Anthopoulos, *Unconventional chemical doping of organic semiconducting materials* **2013**, WO 2013098648 A1.
[43] Y. Han, G. Barnes, Y.-H. Lin, J. Martin, M. Al-Hashimi, S. Y. AlQaradawi, T. D. Anthopoulos, M. Heeney, *Chemistry of Materials* **2016**, DOI: 10.1021/acs.chemmater.6b03761.
[44] B. Lüssem, C.-M. Keum, D. Kasemann, B. Naab, Z. Bao, K. Leo, *Chemical Reviews* **2016**, DOI: 10.1021/acs.chemrev.6b00329.
[45] D. K. Hwang, C. Fuentes-Hernandez, J. D. Berrigan, Y. Fang, J. Kim, W. J. Potscavage, Jr., H. Cheun, K. H. Sandhage, B. Kippelen, *Journal of Materials Chemistry* **2012**, 22, 5531.

[46] D. Guo, T. Miyadera, S. Ikeda, T. Shimada, K. Saiki, *Journal of Applied Physics* **2007**, 102, 023706.
[47] C. D. Dimitrakopoulos, P. R. L. Malenfant, *Advanced Materials* **2002**, 14, 99.
[48] I. McCulloch, M. Heeney, C. Bailey, K. Genevicius, I. MacDonald, M. Shkunov, D. Sparrowe, S. Tierney, R. Wagner, W. Zhang, M. L. Chabinyc, R. J. Kline, M. D. McGehee, M. F. Toney, *Nat Mater* **2006**, 5, 328.
[49] R. Hamilton, J. Smith, S. Ogier, M. Heeney, J. E. Anthony, I. McCulloch, J. Veres, D. D. C. Bradley, T. D. Anthopoulos, *Advanced Materials* **2009**, 21, 1166.
[50] J. Smith, W. M. Zhang, R. Sougrat, K. Zhao, R. P. Li, D. K. Cha, A. Amassian, M. Heeney, I. McCulloch, T. D. Anthopoulos, *Advanced Materials* **2012**, 24, 2441.
[51] K. Zhao, O. Wodo, D. Ren, H. U. Khan, M. R. Niazi, H. Hu, M. Abdelsamie, R. Li, E. Q. Li, L. Yu, B. Yan, M. M. Payne, J. Smith, J. E. Anthony, T. D. Anthopoulos, S. T. Thoroddsen, B. Ganapathysubramanian, A. Amassian, *Advanced Functional Materials* **2016**, 26, 1737.
[52] S. Hunter, T. D. Anthopoulos, *Advanced Materials* **2013**, 25, 4320.
[53] P. Pingel, R. Schwarzl, D. Neher, *Applied Physics Letters* **2012**, 100.
[54] E. F. Aziz, A. Vollmer, S. Eisebitt, W. Eberhardt, P. Pingel, D. Neher, N. Koch, *Advanced Materials* **2007**, 19, 3257.
[55] M. Pfeiffer, K. Leo, X. Zhou, J. S. Huang, M. Hofmann, A. Werner, J. Blochwitz-Nimoth, *Organic Electronics* **2003**, 4, 89.
[56] S. Olthof, S. Mehraeen, S. K. Mohapatra, S. Barlow, V. Coropceanu, J.-L. Brédas, S. R. Marder, A. Kahn, *Physical Review Letters* **2012**, 109, 176601.
[57] M. L. Tietze, L. Burtone, M. Riede, B. Lüssem, K. Leo, *Physical Review B* **2012**, 86, 035320.
[58] G. Gelinck, P. Heremans, K. Nomoto, T. D. Anthopoulos, *Advanced Materials* **2010**, 22, 3778.
[59] F. Li, A. Nathan, Y. Wu, B. S. Ong, *Organic Thin Film Transistor Integration: A Hybrid Approach*, Wiley, **2011**.
[60] G. Schmid, R. Waser, *Nanotechnology: Volume 4: Information Technology II*, Wiley, **2008**.
[61] G. Horowitz, R. Hajlaoui, H. Bouchriha, R. Bourguiga, M. Hajlaoui, *Advanced Materials* **1998**, 10, 923.
[62] G. Horowitz, *Advanced Functional Materials* **2003**, 13, 53.
[63] P. Stallinga, H. L. Gomes, *Organic Electronics* **2006**, 7, 592.
[64] W. L. Kalb, B. Batlogg, *Physical Review B* **2010**, 81, 035327.
[65] M. Grünewald, P. Thomas, D. Würtz, *physica status solidi (b)* **1980**, 100, K139.
[66] S. Hunter, A. D. Mottram, T. D. Anthopoulos, *Journal of Applied Physics* **2016**, 120, 025502.
[67] S. D. Wang, T. Minari, T. Miyadera, Y. Aoyagi, K. Tsukagoshi, *Applied Physics Letters* **2008**, 92.
[68] R. Ahmed, C. Simbrunner, G. Schwabegger, M. A. Baig, H. Sitter, *Applied Physics a-Materials Science & Processing* **2014**, 117, 2235.
[69] Y. Yan, X. J. She, H. Zhu, S. D. Wang, *Organic Electronics* **2011**, 12, 823.
[70] H. Sinno, S. Fabiano, X. Crispin, M. Berggren, I. Engquist, *Applied Physics Letters* **2013**, 102, 113306.
[71] P. Wei, J. H. Oh, G. Dong, Z. Bao, *J. Am. Chem. Soc.* **2010**, 132, 8852.
[72] C. Pitsalidis, A. M. Pappa, S. Hunter, A. Laskarakis, T. Kaimakamis, M. M. Payne, J. E. Anthony, T. D. Anthopoulos, S. Logothetidis, *Journal of Materials Chemistry C* **2016**, 4, 3499.
[73] K. K. Ryu, I. Nausieda, D. D. He, A. I. Akinwande, V. Bulovic, C. G. Sodini, *IEEE Transactions on Electron Devices* **2010**, 57, 1003.

[74] J. C. Scott, *Journal of Vacuum Science & Technology A* **2003**, 21, 521.
[75] A. Kahn, N. Koch, W. Gao, *Journal of Polymer Science Part B: Polymer Physics* **2003**, 41, 2529.
[76] E. G. Bittle, J. I. Basham, T. N. Jackson, O. D. Jurchescu, D. J. Gundlach, *Nature communications* **2016**, 7.
[77] C. Vanoni, S. Tsujino, T. A. Jung, *Applied Physics Letters* **2007**, 90, 193119.
[78] E. Meijer, G. Gelinck, E. Van Veenendaal, B.-H. Huisman, D. De Leeuw, T. Klapwijk, *Applied physics letters* **2003**, 82, 4576.
[79] J. Smith, R. Hamilton, Y. Qi, A. Kahn, D. D. C. Bradley, M. Heeney, I. McCulloch, T. D. Anthopoulos, *Advanced Functional Materials* **2010**, 20, 2330.
[80] V. Vinciguerra, M. La Rosa, D. Nicolosi, G. Sicurella, L. Occhipinti, *Organic electronics* **2009**, 10, 1074.
[81] Y. Diao, B. C. K. Tee, G. Giri, J. Xu, D. H. Kim, H. A. Becerril, R. M. Stoltenberg, T. H. Lee, G. Xue, S. C. B. Mannsfeld, Z. N. Bao, *Nat Mater* **2013**, 12, 665.
[82] H. C. Yang, T. J. Shin, L. Yang, K. Cho, C. Y. Ryu, Z. N. Bao, *Advanced Functional Materials* **2005**, 15, 671.
[83] C.-T. Lee, H.-C. Chen, *Organic Electronics* **2011**, 12, 1852.
[84] S. P. Tiwari, W. J. Potscavage, Jr., T. Sajoto, S. Barlow, S. R. Marder, B. Kippelen, *Organic Electronics* **2010**, 11, 860.
[85] C. L. Fan, W. C. Lin, H. S. Chang, Y. Z. Lin, B. R. Huang, *Materials* **2016**, 9.
[86] J. Li, X.-W. Zhang, L. Zhang, H. Khizar ul, X.-Y. Jiang, W.-Q. Zhu, Z.-L. Zhang, *Solid State Communications* **2009**, 149, 1826.
[87] F. Ante, D. Kaelblein, U. Zschieschang, T. W. Canzler, A. Werner, K. Takimiya, M. Ikeda, T. Sekitani, T. Someya, H. Klauk, *Small* **2011**, 7, 1186.
[88] B. Lee, T. Choi, S.-W. Cheong, V. Podzorov, *Advanced Functional Materials* **2009**, 19, 3726.
[89] A. Das, R. Dost, T. H. Richardson, M. Grell, D. C. Wedge, D. B. Kell, J. J. Morrison, M. L. Turner, *Sensors and Actuators B: Chemical* **2009**, 137, 586.
[90] T. Toccoli, A. Pallaoro, M. Tonezzer, N. Coppedè, S. Iannotta, *Solid-State Electronics* **2008**, 52, 417.
[91] S. Wo, R. L. Headrick, J. E. Anthony, *Journal of Applied Physics* **2012**, 111, 073716.
[92] M. R. Niazi, R. Li, M. Abdelsamie, K. Zhao, D. H. Anjum, M. M. Payne, J. Anthony, D.-M. Smilgies, A. Amassian, *Advanced Functional Materials* **2015**, DOI: 10.1002/adfm.201502428n/a.
[93] O. D. Jurchescu, J. Baas, T. T. M. Palstra, *Applied Physics Letters* **2004**, 84, 3061.
[94] L. H. Jimison, M. F. Toney, I. McCulloch, M. Heeney, A. Salleo, *Advanced Materials* **2009**, 21, 1568.
[95] M. R. Niazi, R. Li, E. Qiang Li, A. R. Kirmani, M. Abdelsamie, Q. Wang, W. Pan, M. M. Payne, J. E. Anthony, D.-M. Smilgies, S. T. Thoroddsen, E. P. Giannelis, A. Amassian, *Nature communications* **2015**, 6, 8598.
[96] H. Klauk, *Organic Electronics: Materials, Manufacturing, and Applications*, Wiley, **2006**.
[97] H. Kleemann, C. Schuenemann, A. A. Zakhidov, M. Riede, B. Luessem, K. Leo, *Organic Electronics* **2012**, 13, 58.
[98] P. Pahner, H. Kleemann, L. Burtone, M. L. Tietze, J. Fischer, K. Leo, B. Lüssem, *Physical Review B* **2013**, 88, 195205.
[99] G. Gbabode, M. Dohr, C. Niebel, J.-Y. Balandier, C. Ruzié, P. Négrier, D. Mondieig, Y. H. Geerts, R. Resel, M. Sferrazza, *ACS Applied Materials & Interfaces* **2014**, 6, 13413.
[100] A. Tarasov, S. Zhang, M.-Y. Tsai, P. M. Campbell, S. Graham, S. Barlow, S. R. Marder, E. M. Vogel, *Adv. Mater.* **2015**, 27, 1175.

[101] a) A. R. Kirmani, A. Kiani, M. M. Said, O. Voznyy, N. Wehbe, G. Walters, S. Barlow, E. H. Sargent, S. R. Marder, A. Amassian, *ACS Energy Letters* **2016**, 1, 922; b) S. A. Paniagua, J. Baltazar, H. Sojoudi, S. K. Mohapatra, S. Zhang, C. L. Henderson, S. Graham, S. Barlow, S. R. Marder, *Materials Horizons* **2014**, 1, 111.
[102] A. R. Kirmani, F. P. García de Arquer, J. Z. Fan, J. I. Khan, G. Walters, S. Hoogland, N. Wehbe, M. M. Said, S. Barlow, F. Laquai, S. R. Marder, E. H. Sargent, A. Amassian, *ACS Energy Letters* **2017**, 2, 1952.
[103] X. Lin, G. E. Purdum, Y. Zhang, S. Barlow, S. R. Marder, Y.-L. Loo, A. Kahn, *Chemistry of Materials* **2016**, 28, 2677.
[104] J. G. Labram, Y.-H. Lin, T. D. Anthopoulos, *Small* **2015**, 11, 5472.
[105] X. Zhang, H. Bronstein, A. J. Kronemeijer, J. Smith, Y. Kim, R. J. Kline, L. J. Richter, T. D. Anthopoulos, H. Sirringhaus, K. Song, M. Heeney, W. Zhang, I. McCulloch, D. M. DeLongchamp, *Nature communications* **2013**, 4, 2238.
[106] A. V. Kepman, V. F. Sukhoverkhov, A. Tressaud, C. Labrugere, E. Durand, N. S. Chilingarov, L. N. Sidorov, *Journal of Fluorine Chemistry* **2006**, 127, 1455.
[107] Y. Smets, C. B. Stark, F. Schmitt, M. T. Edmonds, S. Lach, C. A. Wright, D. P. Langley, K. J. Rietwyk, A. Schenk, A. Tadich, M. Wanke, C. Ziegler, L. Ley, C. I. Pakes, *Organic Electronics* **2013**, 14, 169.
[108] M. T. Edmonds, M. Wanke, A. Tadich, H. M. Vulling, K. J. Rietwyk, P. L. Sharp, C. B. Stark, Y. Smets, A. Schenk, Q. H. Wu, L. Ley, C. I. Pakes, *Journal of Chemical Physics* **2012**, 136, 124701.
[109] A. Tadich, M. T. Edmonds, L. Ley, F. Fromm, Y. Smets, Z. Mazej, J. Riley, C. I. Pakes, T. Seyller, M. Wanke, *Applied Physics Letters* **2013**, 102, 241601.
[110] K. J. Rietwyk, M. Wanke, H. M. Vulling, M. T. Edmonds, P. L. Sharp, Y. Smets, Q. H. Wu, A. Tadich, S. Rubanov, P. J. Moriarty, L. Ley, C. I. Pakes, *Physical Review B* **2011**, 84, 035404.
[111] Y. Yuan, G. Giri, A. L. Ayzner, A. P. Zoombelt, S. C. B. Mannsfeld, J. Chen, D. Nordlund, M. F. Toney, J. Huang, Z. Bao, *Nat. Commun.* **2014**, 5, 3005.
[112] J. H. Park, Y. T. Lee, H. S. Lee, J. Y. Lee, K. Lee, G. B. Lee, J. Han, T. W. Kim, S. Im, *ACS Applied Materials & Interfaces* **2013**, 5, 1625.
[113] D. K. Hwang, C. Fuentes-Hernandez, J. Kim, W. J. Potscavage, S.-J. Kim, B. Kippelen, *Advanced Materials* **2011**, 23, 1293.
[114] D. K. Hwang, C. Fuentes-Hernandez, J. B. Kim, W. J. Potscavage Jr, B. Kippelen, *Organic Electronics* **2011**, 12, 1108.
[115] Y.-H. Kim, J. E. Anthony, S. K. Park, *Organic Electronics* **2012**, 13, 1152.
[116] M. J. Ford, M. Wang, H. Phan, T.-Q. Nguyen, G. C. Bazan, *Adv. Funct. Mater.* **2016**, 26, 4472.

Figures

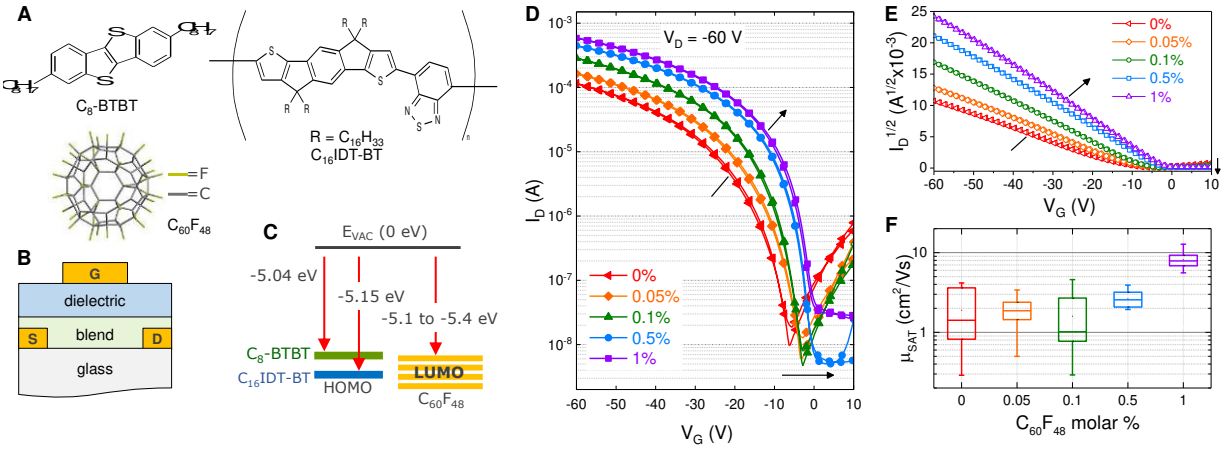

Figure 1. (a) The chemical structures of 2,7-dioctyl[1]benzothieno[3,2-b][1]benzothiophene (C_8-BTBT), indacenodithiophene-benzothiadiazole (C_{16}IDT-BT) and $C_{60}F_{48}$. (b) Top-gate bottom-contact (TG-BC) transistor architecture used to study the various blend formulations. (c) Energy level diagram showing C_8-BTBT and C_{16}IDT-BT HOMO levels measured using air photoemission spectroscopy and compared to the range of published LUMO energies for $C_{60}F_{48}$ [Refs: [107] [108] [109] [110]]. (d) Transfer characteristics for the C_8-BTBT:C_{16}IDT-BT blend transistors with 0, 0.05, 0.1, 0.5 and 1% molar weight $C_{60}F_{48}$ measured at V_D = -60 V. These devices were made at the same time under the same processing conditions, to demonstrate the general trend in the transfer characteristics with increasing addition of the *p*-dopant. The channel length and width of all of the transistors are 80 µm and 1000 µm, respectively. (e) The corresponding $\sqrt{I_D}$ vs. V_G plots. (f) Saturation mobility histogram constructed from 10 C_8-BTBT:C_{16}IDT-BT blend OTFTs with different dopant concentrations (0, 0.05, 0.1, 0.5 and 1% molar weight $C_{60}F_{48}$) showing that statistically the greatest improvement in mobility occurs between 0.5% and 1%.

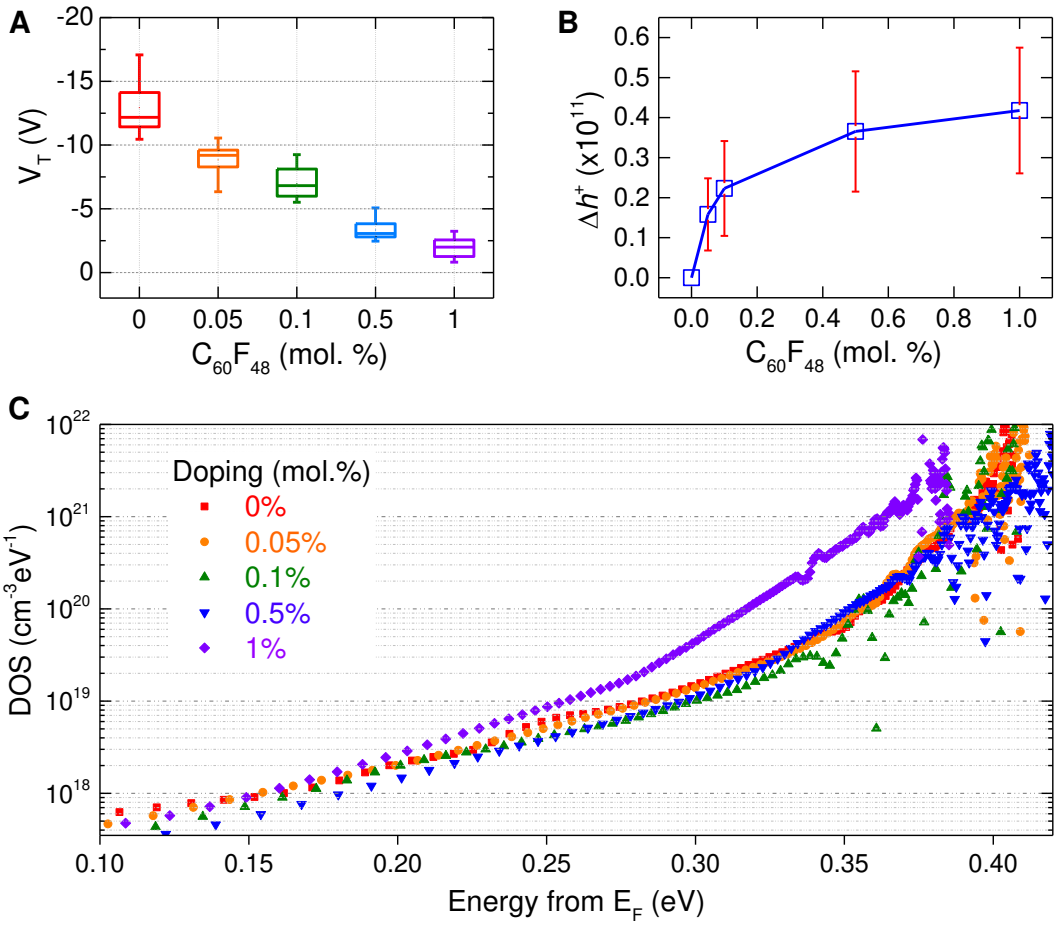

Figure 2. (a) Threshold voltage statistics obtained for 10 C_8-BTBT:C_{16}IDT-BT blend OTFTs with 0, 0.05, 0.1, 0.5 and 1% molar weight $C_{60}F_{48}$. (b) Number of holes (Δh^+) induced in the OTFT channel as a function of dopant concentration in solution. (c) The density of states (DOS) calculated for five blend-based OTFTs with dopant concentration varying from 0 to 1% mol. wt. $C_{60}F_{48}$. The origin of the energy axis is the Fermi energy level (E_F) at thermal equilibrium which corresponds to the flat-band voltage of the transistors.

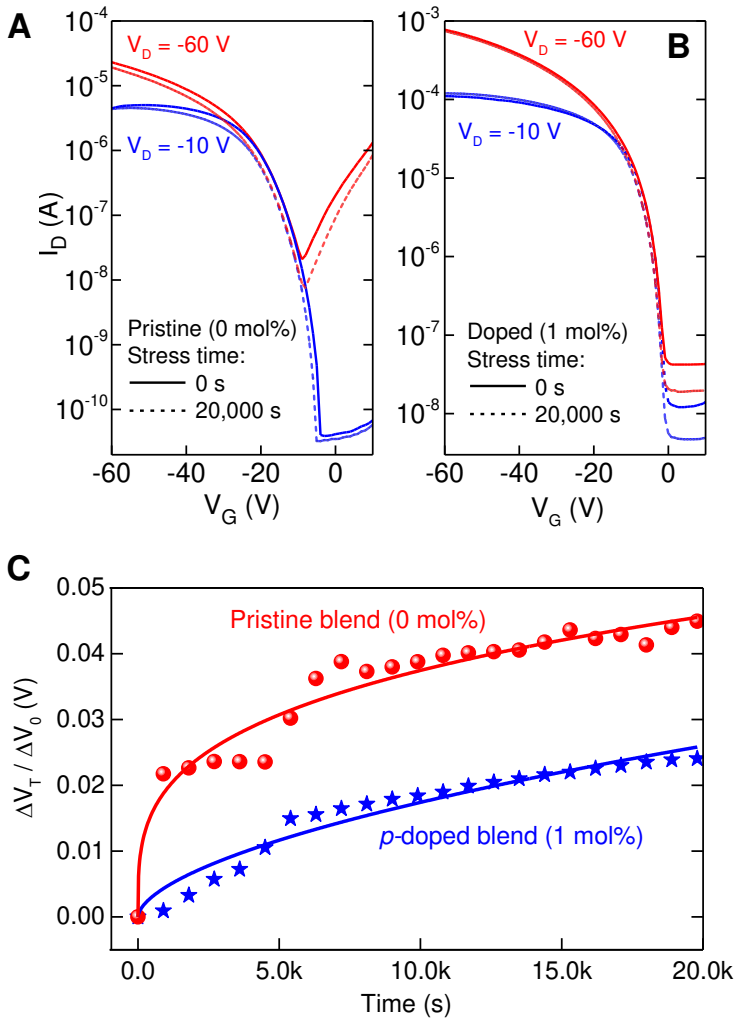

Figure 3. Transfer characteristics of blend OTFTs before and after 20,000 s of constant gate bias (V_G = -40 V) and drain bias (V_G = -10 V) application for: (a) the pristine C_8-BTBT:C_{16}IDT-BT blend, and (b) C_8-BTBT:C_{16}IDT-BT:$C_{60}F_{48}$(1% mol%). The devices have channel length and width of 80 µm and 1000 µm, respectively, and were tested in nitrogen atmosphere. (c) Experimental data (symbols) and stretched exponential fittings (lines) used to extrapolate the β and τ parameters for the pristine (C_8-BTBT:C_{16}IDT-BT) and *p*-doped (C_8-BTBT:C_{16}IDT-BT:$C_{60}F_{48}$(1%) blend devices.

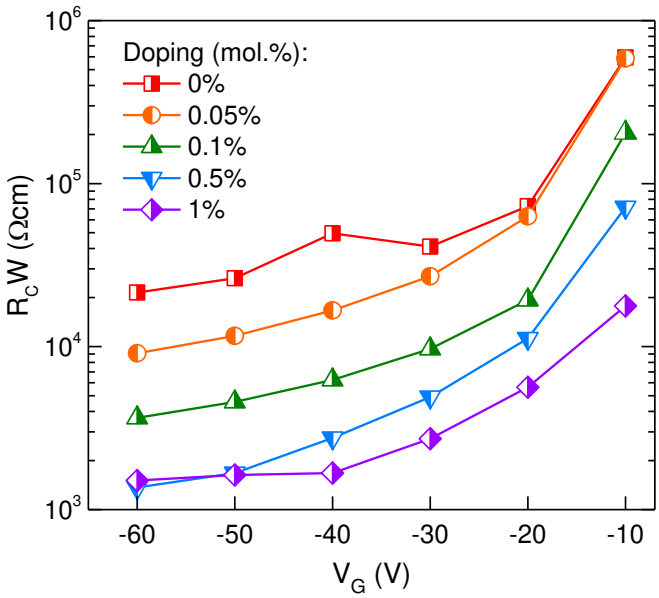

Figure 4. Channel width-normalised contact resistance (R_CW) as a function of gate bias, calculated for the C_8-BTBT:C_{16}IDT-BT blend TFTs with 0, 0.05, 0.1, 0.5 and 1% molar weight $C_{60}F_{48}$.

 DOI: 10.1002/aelm.201700464

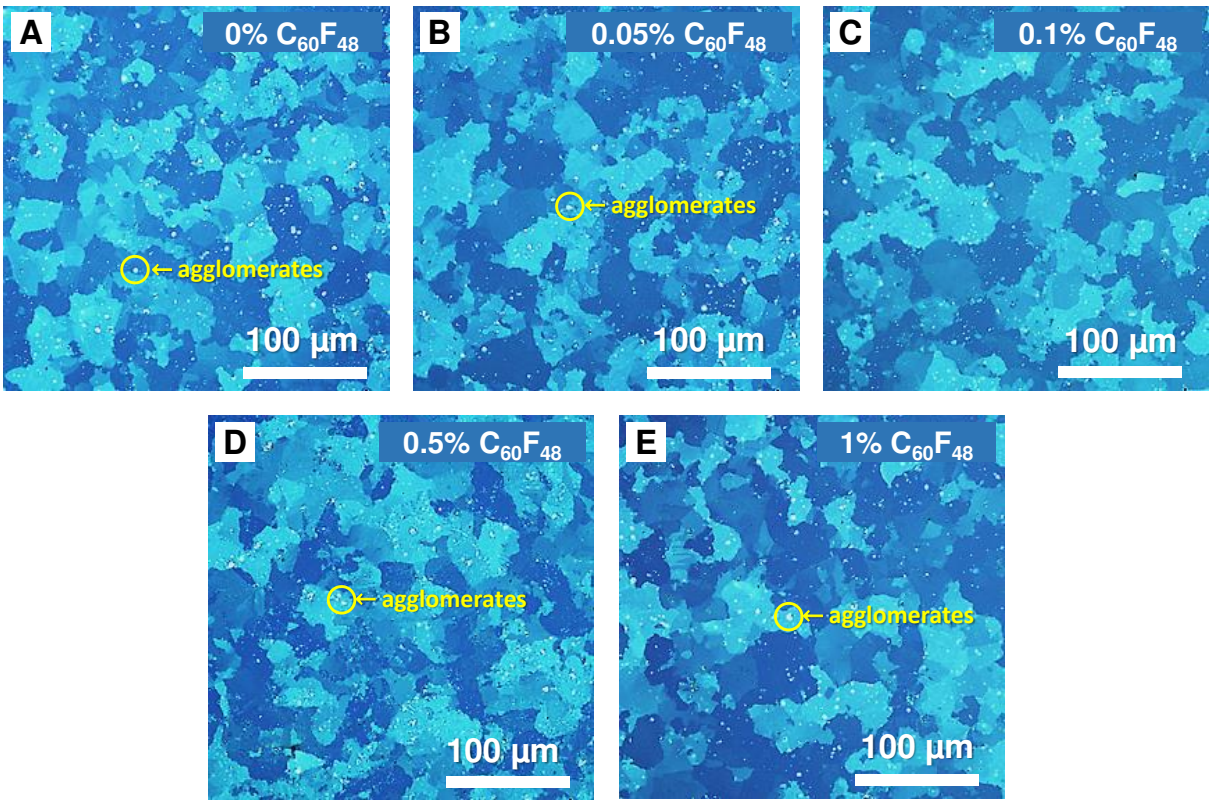

Figure 5. Polarised optical microscope (POM) images of the C_8-BTBT:C_{16}IDT-BT blend with varying amounts of dopant, $C_{60}F_{48}$: a) 0%, b) 0.05%, c) 0.1%, d) 0.5%, e) 1%.

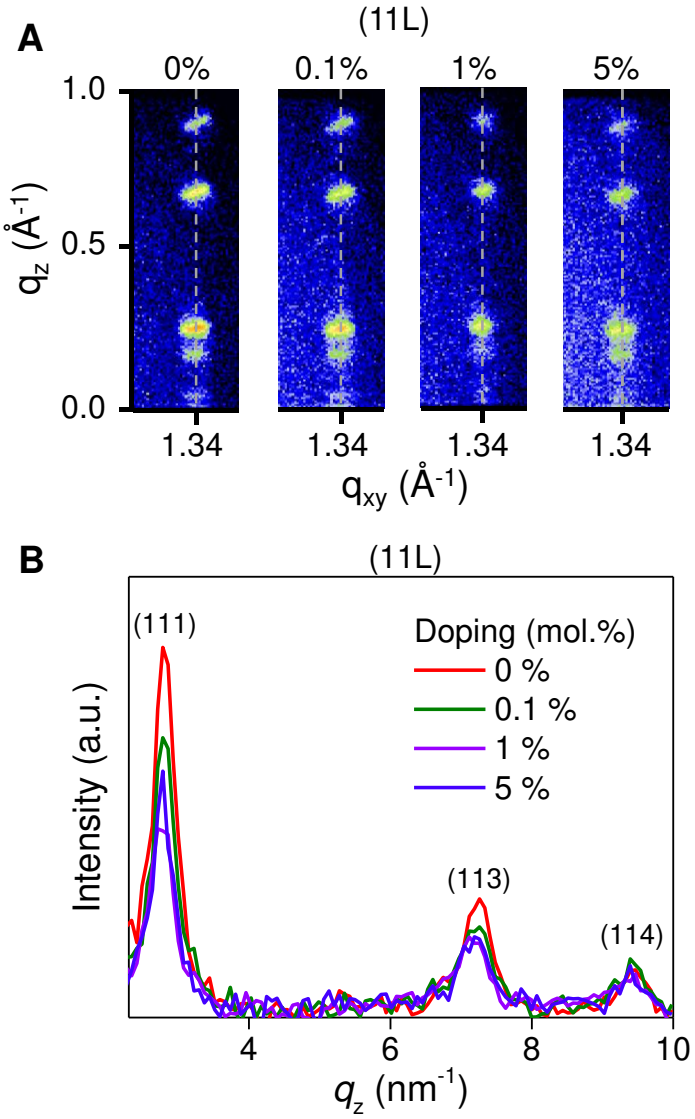

Figure 6. Grazing incidence wide angle X-ray scattering (GIWAXS) data showing in-plane structures for various doped C_8-BTBT:C_{16}IDT-BT blend films (0%, 0.1%, 1% and 5% mol. wt. $C_{60}F_{48}$), where (a) compares the q_{xy} position, with the dashed line highlighting that there is no shift in the in-plane peak. (b) Shows that there is also no shift in the q_z values, suggesting that crystal packing is not altered by the presence of the $C_{60}F_{48}$.

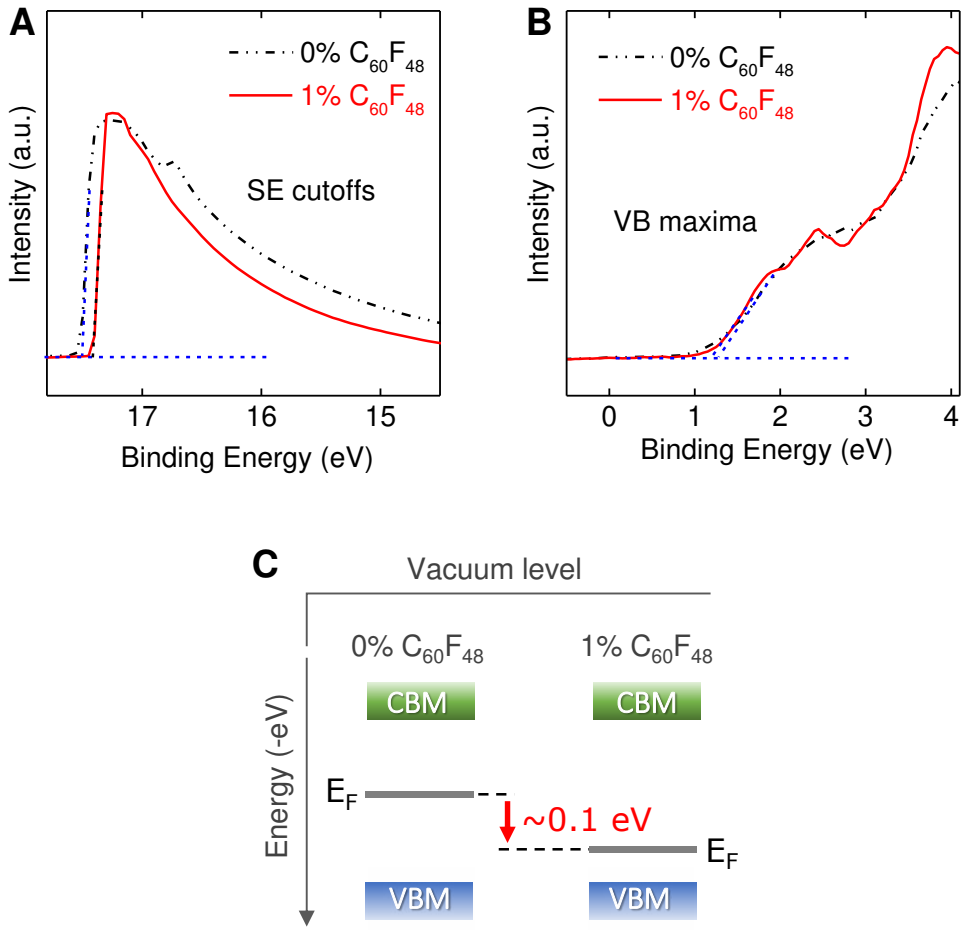

Figure 7. Ultra-violet photoelectron spectroscopy (UPS) data obtained for the pristine C_8-BTBT:C_{16}IDT-BT and *p*-doped C_8-BTBT:C_{16}IDT-BT:$C_{60}F_{48}$(1%) blends. (a) Secondary-electron (SE) cut-offs, and (b) valance band maxima (VBM) spectra. (c) Corresponding energy band diagram reconstructed by considering an arbitrary band gap of 1.5 eV in order to calculate the position of the conduction band minima (CBM). E_F is found to shift towards the VBM by ~0.1 eV upon doping with 1% $C_{60}F_{48}$ (energy not in scale).

Table 1. A summary of the literature on bias-stress stability for blend OTFTs.

Active material	Process Temp. [°C]	Mobility [cm^2/Vs]	Dielectric material	Geometric capacitance [nF/cm^2]	Gate stress [V]	Drain stress [V]	Electric flux density [C/cm^2]	Stress time [s]	ΔV_{th} [V]	Traps density [cm^{-2}]	Ref.
C8-BTBT:C16IDT-BT:C60F48(1%)	50	7.8	AF2400	5.28	-40	-10	2.11×10^{-7}	20,000	0.91	3.00×10^{10}	This work
C8-BTBT:C16IDT-BT	50	1.4	AF2400	5.28	-40	-10	2.11×10^{-7}	20,000	1.34	4.42×10^{10}	
C8-BTBT:PS	100	25	PVP:HDA	12	-15	0	1.80×10^{-7}	3,000	~5	3.75×10^{11}	[111]
TIPS-pentacene/i-PMMA	110	n/a	Al_2O_3	~80	-15	0	1.20×10^{-6}	5,000	3	1.50×10^{12}	[112]
TIPS-pentacene/PTAA	~100	1.1×10^{-2}	Al_2O_3	78.6	-8	-8	6.29×10^{-7}	3,600	~1.5	7.37×10^{11}	[113]
TIPS-pentacene/PTAA	~100	0.20	CYTOP	2.3	-50	-50	1.15×10^{-7}	3,600	~2	2.88×10^{10}	[113]
TIPS-pentacene/PTAA	~100	0.52	CYTOP/ Al_2O_3	34.8	-8	-8	2.78×10^{-7}	3,600	~0.4	8.70×10^{10}	[113]
TIPS-pentacene/PTAA	~100	0.24	CYTOP/ Al_2O_3	34.8	-8	-8	2.78×10^{-7}	7,200	~0.2	4.35×10^{10}	[114]
diF-TESADT:PαMS (2:1)	~90	~0.16	SiO_2	17.3	-20	-0.1	3.46×10^{-7}	7,200	12	1.30×10^{12}	[115]
diF-TESADT:PαMS (2:2)	~90	~0.16	SiO_2	17.3	-20	-0.1	3.46×10^{-7}	7,200	8	8.65×10^{11}	[115]
PCDTPT:$PC_{61}BM$	200	0.5	SiO_2	11.5	-10	-80	1.15×10^{-7}	300	0.8	5.75×10^{10}	[116]
PCDTPT:$PC_{61}BM$	200	0.5	SiO_2	11.5	-30	-80	3.45×10^{-7}	300	0.2	1.44×10^{10}	[116]
diF-TESADT:PTAA	120	1.7	CYTOP	2.1	-50	-50	1.05×10^{-7}	18,000	10	1.31×10^{11}	[72]

Introducing a molecular *p*-dopant into an organic small-molecule/polymer blend is shown to improve the hole mobility and bias-stress stability of the resulting transistors. This simple approach is shown to harnesses the benefits of *p*-doping without adverse effects on the channel microstructure, hence overcoming an important limitation for the practical utilization of molecular dopants in organic transistors.

The Impact of Molecular *p*-Doping on Charge Transport in High Mobility Small-Molecule/Polymer Blend Organic Transistors

Alexandra F. Paterson, Yen-Hung Lin, Alexander D. Mottram, Zhuping Fei, Muhammad R. Niazi, Ahmad R. Kirmani, Aram Amassian, Olga Solomeshch, Nir Tessler, Martin Heeney, Thomas D. Anthopoulos

The Impact of Molecular *p*-Doping on Charge Transport in High Mobility Small-Molecule/Polymer Blend Organic Transistors

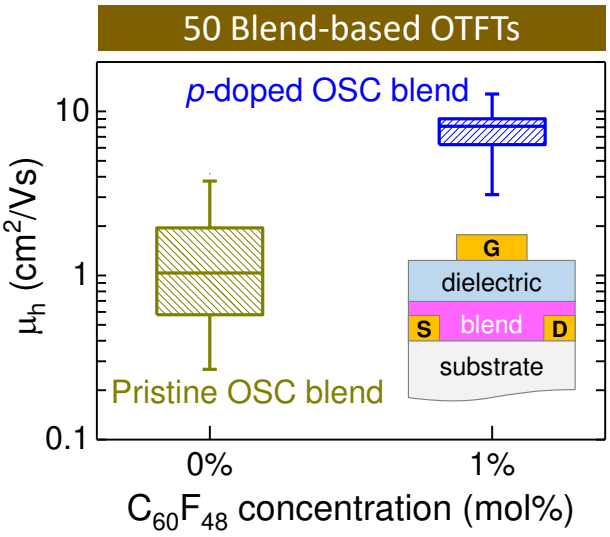

Adv. Electron. Mater. **2017**, *1700464,* **DOI:** 10.1002/aelm.201700464

Supporting Information

The Impact of Molecular *p*-Doping on Charge Transport in High Mobility Small-Molecule/Polymer Blend Organic Transistors

*Alexandra F. Paterson, Yen-Hung Lin, Alexander D. Mottram, Zhuping Fei, Muhammad R. Niazi, Ahmad R. Kirmani, Aram Amassian, Olga Solomeshch, Nir Tessler, Martin Heeney, Thomas D. Anthopoulos**

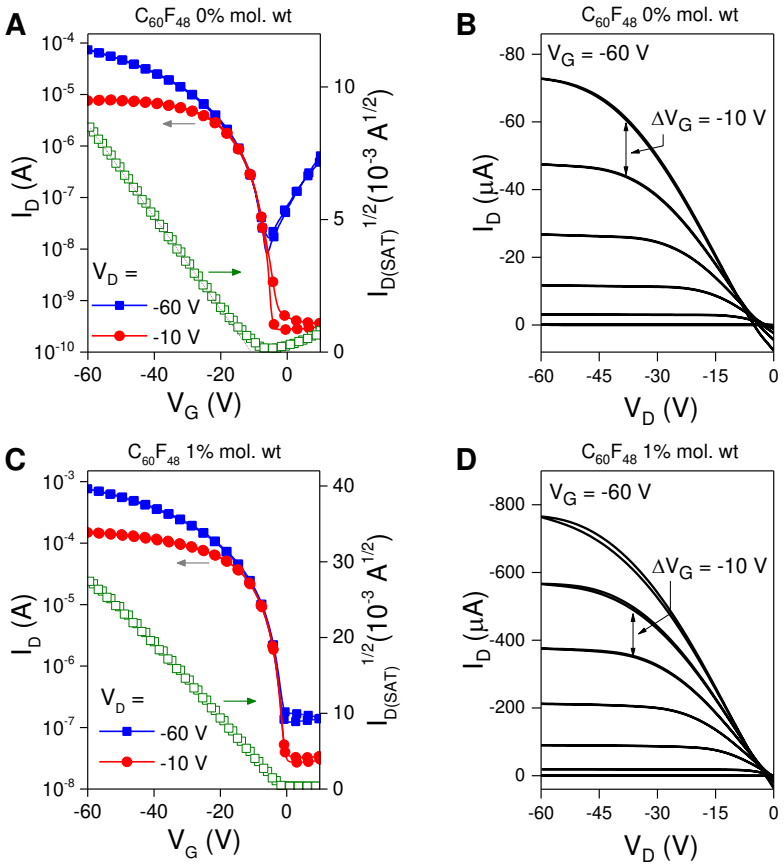

Figure S1. Representative (a) transfer and (b) output characteristics of the pristine C_8-BTBT:C_{16}IDT-BT blend; and representative (c) transfer and (d) output characteristics of the C_8-BTBT:C_{16}IDT-BT:$C_{60}F_{48}$(1%) blend. The transfer characteristics shown here demonstrate the general trend of changes between the pristine and 1% mol. wt. *p*-doped blend systems, for devices with the same channel dimensions fabricated in parallel. General observations from the optimized *p*-doping include: a characteristic increase in the channel on-current, a shift in V_T towards more positive voltages and complete suppression of electron transport. The 3G blend OTFTs are made using gold source/drain electrodes, with Teflon™ AF2400 as a polymer dielectric layer, and the channel lengths and widths are 80 µm and 1000 µm, respectively.

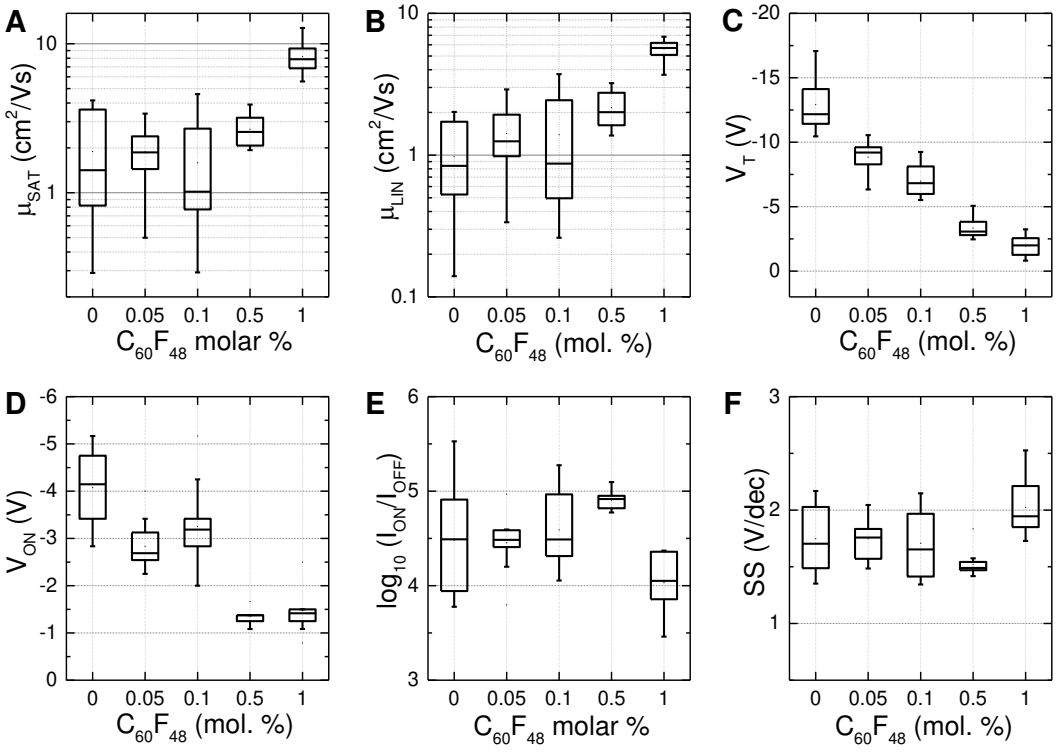

Figure S2. OTFT operating parameters taken over 10 devices for C_8-BTBT:C_{16}IDT-BT blends *p*-doped with 0, 0.05, 0.1, 0.5 and 1% molar weight $C_{60}F_{48}$: (a) saturation mobility, (b) linear mobility, (c) threshold voltage, (d) on voltage, (e) on-off current, (f) subthreshold slope.

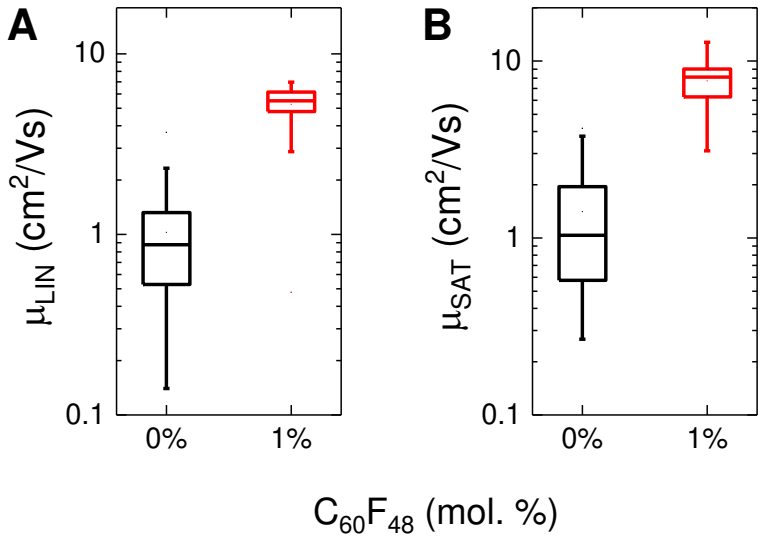

Figure S3. Saturation and linear mobilities from 50 blend OTFTs of the best performing C_8-BTBT:C_{16}IDT-BT:$C_{60}F_{48}$(1%) blend compared to 50 blend OTFTs of the pristine C_8-BTBT:C_{16}IDT-BT blend.

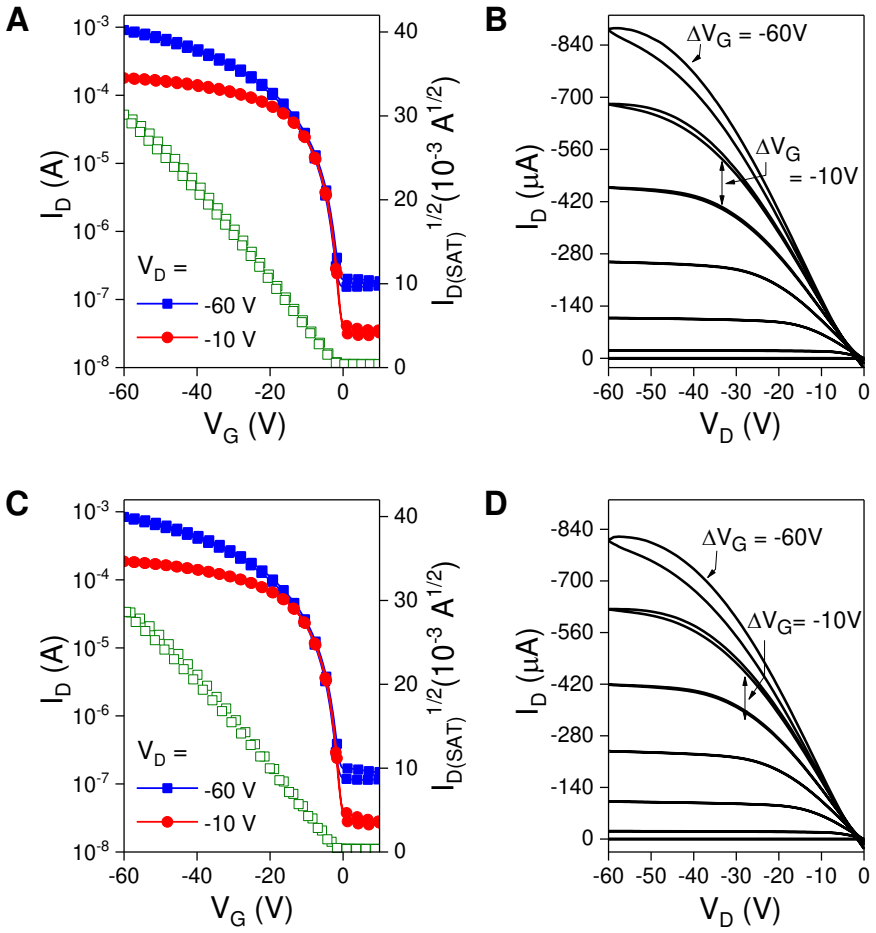

Figure S4. Transfer and output characteristics of the C_8-BTBT:C_{16}IDT-BT:$C_{60}F_{48}$(1%) blend OTFTs, made using Au source/drain electrodes and Teflon™ AF2400 as the polymer dielectric. The transistor in (a) and (b) has channel length 100 μm and with width 1000 μm, and a mobility of 12.8 cm^2/Vs. This device is representative of the maximum performing devices in the 1% $C_{60}F_{48}$ saturation mobility box-and-whisker plot in **Figure S3**. The transistor in (c) and (d) has channel length 80 μm and with width 1000 μm, and has a mobility of 8.9 cm^2/Vs. The latter device represents the upper quartile in the 1% $C_{60}F_{48}$ saturation mobility box-and-whisker plot in **Figure S3**.

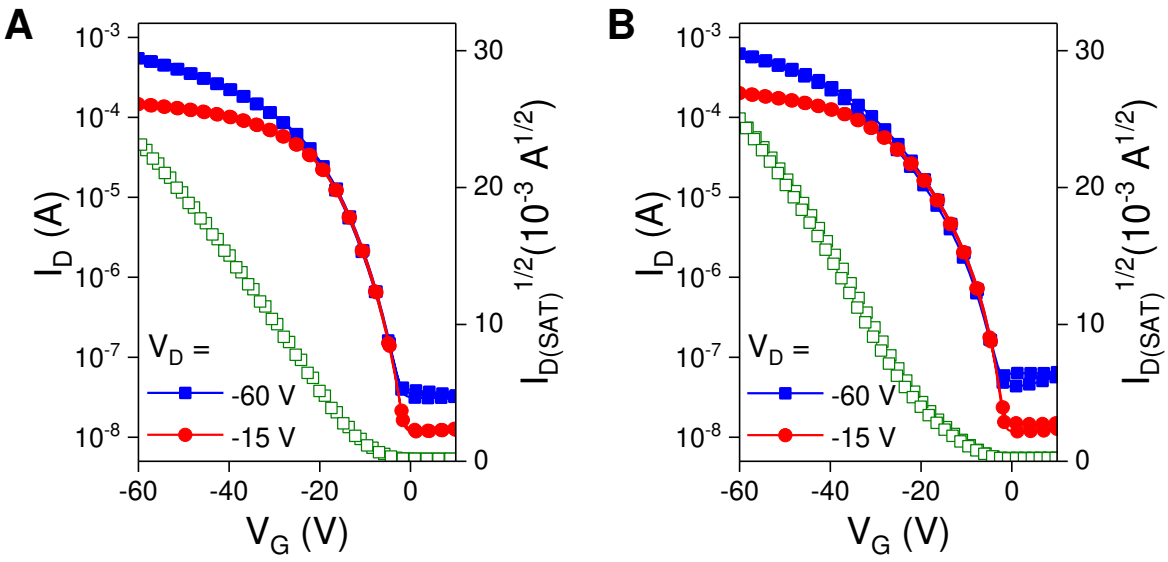

Figure S5. Transfer characteristics of the C_8-BTBT:C_{16}IDT-BT:$C_{60}F_{48}$(1%) blend OTFTs, made using Au source/drain electrodes and Teflon™ AF2400 as a polymer gate dielectric. The device channel dimensions are (a) length 80 µm, width 1000 µm and (b) length 50 µm, width 1000 µm. The hole mobility values are (a) 7.7 cm^2/Vs and (b) 6.9 cm^2/Vs . This data represent the median devices in the 1% $C_{60}F_{48}$ saturation mobility box-and-whisker plot in Figure S3.

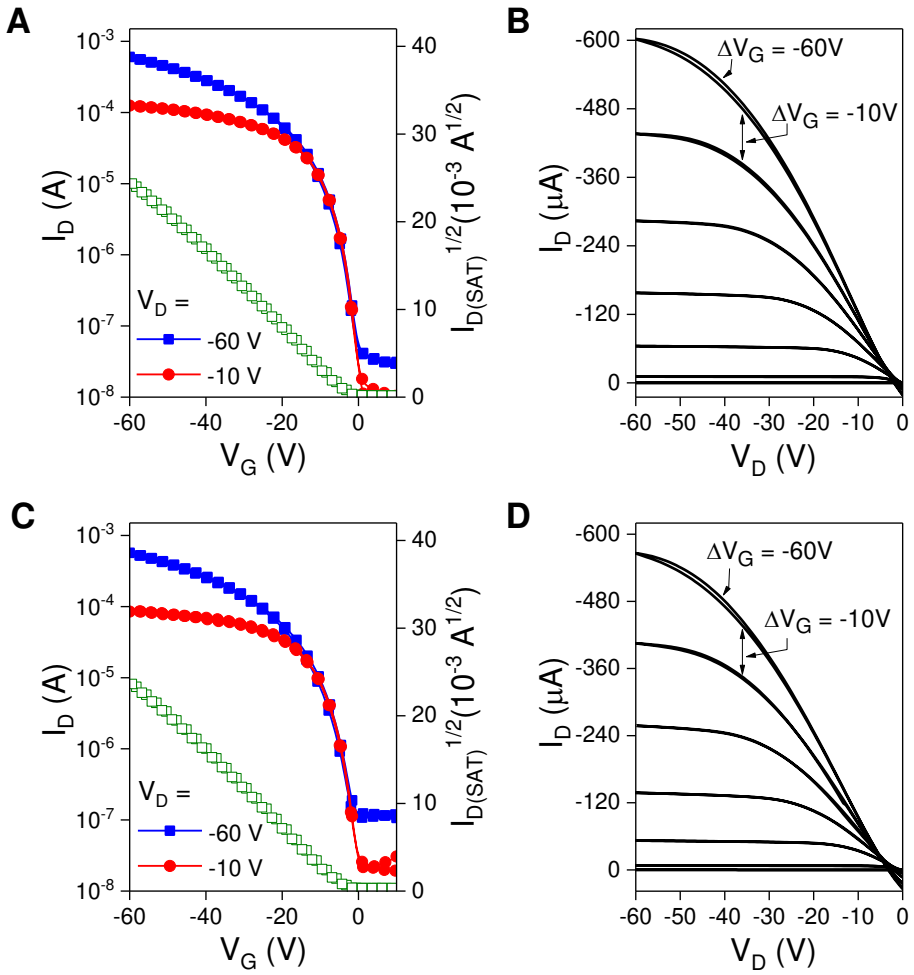

Figure S6. Transfer and output characteristics of the C_8-BTBT:C_{16}IDT-BT:$C_{60}F_{48}$(1%) blend OTFTs, made using gold source/drain electrodes and Teflon™ AF2400 as a polymer dielectric layer. The transistor in (a) and (b) has channel length 80 µm and width 1000 µm, and mobility of 5.4 cm^2/Vs, thereby representing the lower quartile in the 1% $C_{60}F_{48}$ saturation mobility box-and-whisker plot in Figure S3. The transistor in (c) and (d) has channel length 40 µm and width 1000 µm, with a mobility 3.1 cm^2/Vs. The latter data represents the lowest performing devices in the 1% $C_{60}F_{48}$ saturation mobility box-and-whisker plot in Figure S3.

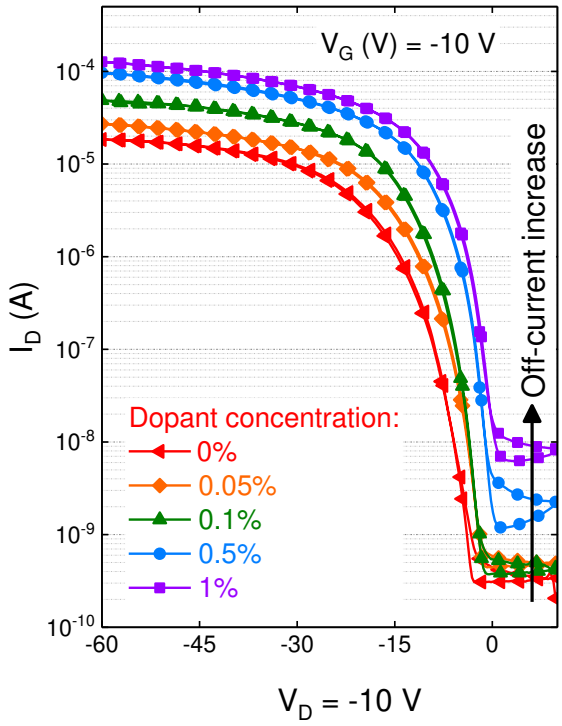

Figure S7. Transfer characteristics for the C_8-BTBT:C_{16}IDT-BT blend with 0, 0.05, 0.1, 0.5 and 1% molar weight $C_{60}F_{48}$ at V_D = -10 V, demonstrating an increase in I_{OFF} at 0.5%.

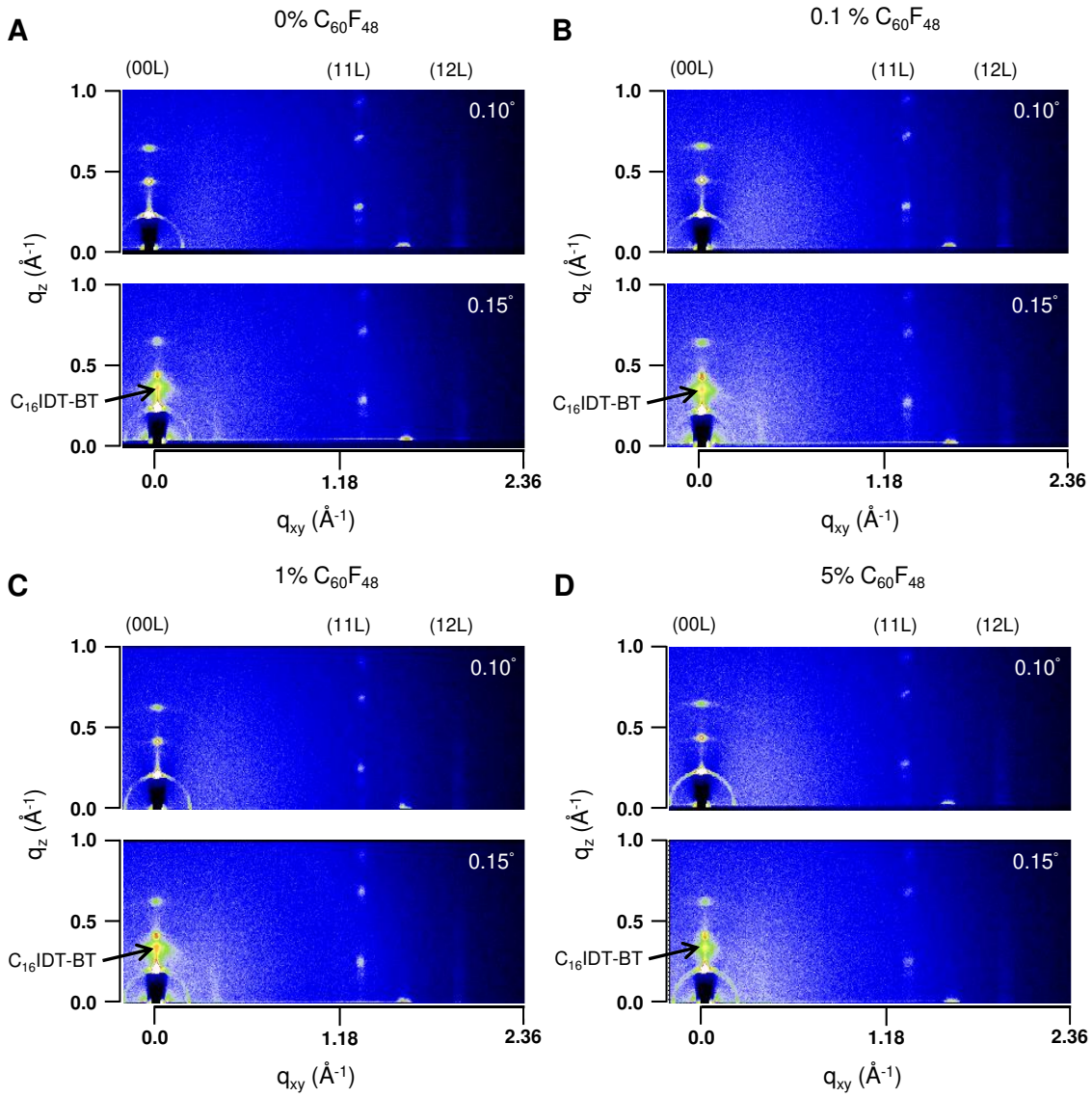

Figure S8. Grazing incidence wide angle X-ray scattering (GIWAXS) data for C_8-BTBT:C_{16}IDT-BT blend films *p*-doped at (a) 0%, (b) 0.1%, (c) 1% and (d) 5% mol. wt. $C_{60}F_{48}$ blends are shown at two grazing incidence angles, 0.10° and 0.15°.

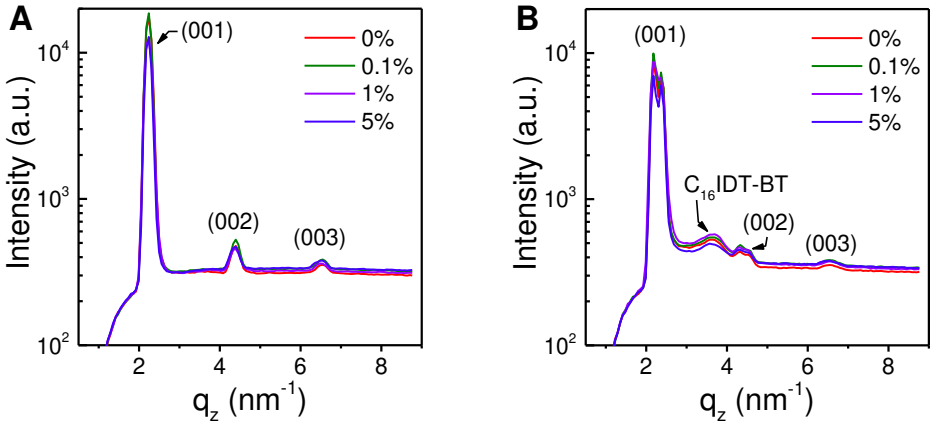

Figure S9. Grazing incidence wide angle X-ray scattering (GIWAXS) data showing intensity vs. q_z for various doped C_8-BTBT:C_{16}IDT-BT blend films (0, 0.1, 1 and 5% mol. wt. $C_{60}F_{48}$) at two different angles of incidence: (a) below the critical angle (0.10°), and (b) the critical angle (0.15°). The peak associated with the C_{16}IDT-BT is only present in (b), indicating that the polymer is not present at the surface/air interface.

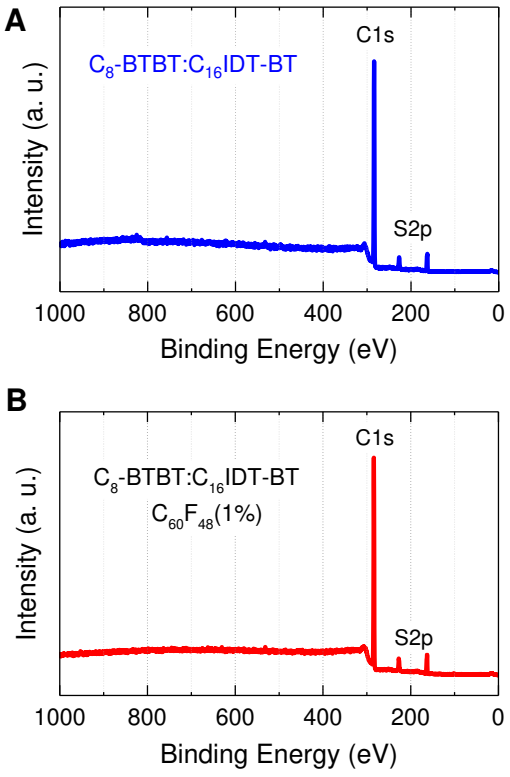

Figure S10. X-ray photoemission spectroscopy (XPS) survey spectra for (a) pristine C_8-BTBT:C_{16}IDT-BT and (b) best performing *p*-doped C_8-BTBT:C_{16}IDT-BT:$C_{60}F_{48}$(1%) ternary blend films.

Table S1. Summary of transistor parameters for C_8-BTBT:C_{16}IDT-BT blend with 0, 0.05, 0.1, 0.5 and 1% molar weight $C_{60}F_{48}$: linear mobility, saturation mobility, threshold voltage, on voltage, subthreshold slope and on-off current ratio.

μ_L [cm^2/Vs]									
0%		0.05%		0.1%		0.5%		1%	
Average	Min-Max	Average	Min-Max	Average	Min-Max	Average	Min-Max	Average	Min-Max
1.0	0.1-2.0	1.4	0.3-2.9	1.4	0.3-3.7	2.2	1.4-3.2	5.6	3.7-6.8
μ_S [cm^2/Vs]									
0%		0.05%		0.1%		0.5%		1%	
Average	Min-Max	Average	Min-Max	Average	Min-Max	Average	Min-Max	Average	Min-Max
1.9	0.3-4.2	1.9	0.5-3.4	1.6	0.3-4.6	2.7	1.9-3.9	8.2	5.6-12.8
Modulus V_T [V]									
0%		0.05%		0.1%		0.5%		1%	
Average	Min-Max	Average	Min-Max	Average	Min-Max	Average	Min-Max	Average	Min-Max
13.1	10.5-17.1	8.9	10.5-6.3	7.1	9.2-5.8	3.3	5.1-2.5	1.9	3.2-0.8
Modulus V_{ON} [V]									
0%		0.05%		0.1%		0.5%		1%	
Average	Min-Max	Average	Min-Max	Average	Min-Max	Average	Min-Max	Average	Min-Max
4.1	5.2-2.8	2.8	4.0-2.3	3.3	5.2-2.0	1.4	1.7-1.1	1.5	2.5-0.8
Subthreshold slope [V/dec]									
0%		0.05%		0.1%		0.5%		1%	
Average	Min-Max	Average	Min-Max	Average	Min-Max	Average	Min-Max	Average	Min-Max
1.7	2.2-1.4	1.7	2.0-1.5	1.7	2.1-1.3	1.5	1.8-1.4	2.0	2.5-1.7
$I_{ON/OFF}$									
0%		0.05%		0.1%		0.5%		1%	
Average	Min-Max	Average	Min-Max	Average	Min-Max	Average	Min-Max	Average	Min-Max
7×10^4	6×10^3 - 3×10^5	3×10^4	6×10^3 - 9×10^4	6×10^4	1×10^4 - 2×10^5	8×10^4	6×10^4 - 1×10^5	1×10^4	3×10^3 - 2×10^4

Table S2. Relative atomic concentrations for the pristine C_8-BTBT:C_{16}IDT-BT blend and best performing *p*-doped C_8-BTBT:C_{16}IDT-BT:$C_{60}F_{48}$(1%) ternary blend films measured from high resolution XPS.

Organic blend	**Relative atomic concentration [%]**			
	C	S	O	F
C_8-BTBT:C_{16}IDT-BT	92.8	6.9	0.3	-
C_8-BTBT:C_{16}IDT-BT:$C_{60}F_{48}$(1%)	92.6	6.9	0.4	-